

Solar-driven thermo-photocatalytic CO₂ methanation over a structured RuO₂:TiO₂/SBA-15 nanocomposite at low temperature

Larissa O. Paulista ^{a,b}, Alexandre F.P. Ferreira ^{a,b}, Bruna Castanheira ^c, Maja B. Đolić ^d, Ramiro J. E. Martins ^{a,b,e}, Rui A.R. Boaventura ^{a,b}, Vítor J.P. Vilar ^{a,b,*}, Tânia F.C.V. Silva ^{a,b,*}

^a LSRE-LCM – Laboratory of Separation and Reaction Engineering-Laboratory of Catalysis and Materials, Faculty of Engineering, University of Porto, Rua Dr. Roberto Frias, Porto 4200-465, Portugal

^b ALICE – Associate Laboratory in Chemical Engineering, Faculty of Engineering, University of Porto, Rua Dr. Roberto Frias, Porto 4200-465, Portugal

^c Centro de Engenharia, Modelagem e Ciências Sociais Aplicadas, Federal University of ABC, Av. dos Estados, 5001, Santo André, SP 09210-580, Brazil

^d Faculty of Technology and Metallurgy, University of Belgrade, 4 Karnegijeva Street, Belgrade 11000, Serbia

^e Superior School of Technology and Management, Bragança Polytechnic University, Bragança 5300-253, Portugal



ARTICLE INFO

Keywords:

Solar-assisted CO₂ hydrogenation
Thermo-photocatalysis
Renewable methane production
RuO₂:TiO₂-functionalized SBA
Outstanding UV-Vis-IR light response

ABSTRACT

A new hybrid catalyst composed of mesostructured silica SBA-15 functionalized with TiO₂ and further loaded with RuO₂ was developed to efficiently promote thermo-photocatalytic CO₂ hydrogenation into methane at low temperatures. The catalytic activity was assessed with respect to TiO₂:RuO₂ loading, catalyst dosage, illumination source (polychromatic sunlight and monochromatic LEDs) and power, [H₂]:[CO₂] molar ratio, temperature, and catalyst reusability. The best methanation yields were attained for the RuO_{2(6.4%)}:TiO_{2(16.9%)}/SBA-15 nanocomposite at 150 °C, under simulated sunlight (0.21 W) and stoichiometric [H₂]:[CO₂] molar ratio, reaching a specific CH₄ production rate of 13.6 mmol g_{cat}⁻¹ h⁻¹; 99.8 % selectivity; 96.8 % CO₂ conversion (110-min; 40 mL); and apparent photonic efficiency/quantum yield of 39.5 %/42.1 %. Considering only the active RuO₂:TiO₂ photocatalyst mass (23.3 %), the CH₄ production rate increased to 58.6 mmol g_{active_cat}⁻¹ h⁻¹. Besides, this highly-active photocatalyst featured excellent UV-Vis-IR light absorbance, high surface area, and stability for reuse when moist gas was removed between cycles.

1. Introduction

In the last few decades, a growing trend in fossil fuel consumption and anthropogenic CO₂ emissions has been witnessed, leading to an energy crisis and global warming. The Intergovernmental Panel on Climate Change (IPCC) has warned that urgent actions are needed toward an energy transition pursuing climate change mitigation [1]. Power-to-X (PtX) technologies occur through CO₂ hydrogenation, which can result in X-type products. The current synthetic natural gas (SNG) production approach is based on the synthesis of methane (Sabatier reaction) provided by CO₂ captured and H₂ resulting from power-to-gas technologies through the electrolysis process generated during the excess electricity peak period. The industrial structure is ready to employ methane since it is the most prevalent chemical in natural gas and has a density that allows storage [2]. Therefore, investigations in this area have drawn industries' interest. According to Thema et al. [3]

* Corresponding authors at: LSRE-LCM – Laboratory of Separation and Reaction Engineering-Laboratory of Catalysis and Materials, Faculty of Engineering, University of Porto, Rua Dr. Roberto Frias, Porto 4200-465, Portugal.

E-mail addresses: vilar@fe.up.pt (V.J.P. Vilar), tania.silva@fe.up.pt (T.F.C.V. Silva).

Nomenclature	
$[C_2H_6]_f$	Final molar concentration of ethane (mol L^{-1}).
$[CH_4]_f$	Final molar concentration of methane (mol L^{-1}).
$[CO_2]_0$	Initial molar concentration of carbon dioxide (mol L^{-1}).
$[CO_2]_f$	Final molar concentration of carbon dioxide (mol L^{-1}).
A	Frequency factor.
A_λ	Average absorbance of the ferrioxalate solution at a wavelength λ .
b	Photoreactor light path length (cm).
c	Light velocity ($3.00 \times 10^8 \text{ m s}^{-1}$).
C	Average concentration of the ferrioxalate solution (mol L^{-1}).
$dn(Fe^{2+})/dt$	Number of Fe^{2+} moles formed per irradiation time (mol s^{-1}).
E	Spectral irradiance ($\text{J s}^{-1} \text{ m}^{-2} \text{ nm}^{-1}$).
E_a	Apparent activation energy (kJ mol^{-1}).
$E_{ph,\lambda}$	Photon energy at a wavelength λ (J).
E_p	Spectral photon irradiance ($\text{Einstein s}^{-1} \text{ m}^{-2} \text{ nm}^{-1}$).
E_u	Urbach energy (eV).
f_λ	Apparent fraction of light absorbed by the photocatalyst considering the wavelength λ of a monochromatic illumination source.
$f_{\lambda_f-\lambda_i}$	Average apparent fraction of light absorbed by the photocatalyst considering the wavelength interval of a polychromatic illumination source.
$F(R_\infty)$	Kubelka-Munk function.
h	Planck's constant ($6.63 \times 10^{-34} \text{ J s}$).
K	Absorption coefficient.
k_{CO_2}	Pseudo-first-order kinetic constant as a function of time (min^{-1}).
\dot{k}_{CO_2}	Pseudo-first-order kinetic constant as a function of accumulated energy (L kJ^{-1}).
N_A	Avogadro number ($6.02 \times 10^{23} \text{ mol}^{-1}$).
Pa_λ	Photon flux (Einstein s^{-1}).
$Pa_{280-580}$	Photon flux reaching the photoreactor between 280 and 580 nm determined by ferrioxalate actinometry (Einstein s^{-1}).
$Pa_{280-800}$	Estimated photon flux reaching the photoreactor between 280 and 800 nm (Einstein s^{-1}).
Q	Accumulated energy (kJ L^{-1}).
r_0	Initial CO_2 reduction rate ($\text{mmol L}^{-1} \text{ min}^{-1}$).
R	Universal gas constant ($8.314 \text{ J mol}^{-1} \text{ K}^{-1}$).
R_∞	Absolute reflectance.
RP	Radiant power reaching the photoreactor (J s^{-1}).
$RP_{280-580}$	Radiant power reaching the photoreactor between 280 and 580 nm determined by ferrioxalate actinometry (J s^{-1}).
$RP_{280-800}$	Estimated radiant power reaching the photoreactor between 280 and 800 nm (J s^{-1}).
S	Scattering coefficient.
$S_{C_2H_6}$	Selectivity of ethane (%).
S_{CH_4}	Selectivity of methane (%).
$S_{e,\lambda}$	Relative spectral distribution of the illumination source.
t	Time (min).
T	Temperature (K).
V	Reactor volume (L).
X_{CO_2}	Percentage of CO_2 reactant converted (%).
$Y_{C_2H_6}$	Production yield of ethane (%).
Y_{CH_4}	Production yield of methane (%).
$\Phi_{CO_2}^{APE}$	Apparent photonic efficiency (%).
$\Phi_{CO_2}^{AQY}$	Apparent quantum yield (%).
Φ_λ	Quantum yield of the ferrioxalate actinometer at wavelength λ .
ϵ_λ	Molar absorptivity of the ferrioxalate solution at a wavelength λ ($\text{L mol}^{-1} \text{ cm}^{-1}$).
λ	Wavelength (nm).

mechanism, a recent study has demonstrated 90 % of CO_2 methanation using $\text{SrTiO}_3/\text{RuO}_2$ at 150 °C [11].

Besides, using semiconductors incorporated within porous materials (such as MOFs, zeolites, and mesoporous silica) can provide an attractive platform to hierarchically organise light-harvesting antennae and catalytic centres to achieve CO_2 reduction [12,13]. Mesoporous silica has become a significant class of widely studied ordered materials, with MCM-41 and SBA-15 materials the most described in the literature. However, the SBA-15 mesoporous silica is preferred due to its large pore volume (up to $1 \text{ cm}^3 \text{ g}^{-1}$) and the ability to yield a higher specific surface area ($400\text{--}1000 \text{ m}^2 \text{ g}^{-1}$). In addition to having great potential as a support for the active phase of heterogeneous catalysts, it can also increase light scattering, facilitating mass and photon transport within the catalytic layer [13,14]. Moreover, the semiconductor heterojunction has been used to improve the general characteristics of the photocatalysts [15,16]. Although many papers about the high activity of RuO_2 on photo/electro-reduction of CO_2 have been published [11,17], to the best of our knowledge, no previous study has investigated SBA-15 functionalised with TiO_2 and RuO_2 to promote thermo-photo-assisted CO_2 hydrogenation at low temperature in the gas phase. Dispersing the TiO_2 : RuO_2 photocatalyst in the mesoporous silica SBA-15 could be a promising strategy to foster CO_2 thermo-photoconversion.

Accordingly, this study aimed the development of a novel highly photoactive nanostructured composite, utilizing an SBA-15 support functionalized with RuO_2 : TiO_2 catalytic materials, to boost solar-assisted CO_2 -to- CH_4 conversion via thermo-photocatalysis. The catalytic activity was evaluated under gas phase batch mode to optimize the

CO_2 hydrogenation process, considering various factors: (i) material composition (in terms of TiO_2 and RuO_2 loading), (ii) material dosage; (iii) illumination source (polychromatic sunlight and monochromatic UV and Vis LEDs) and radiant power (reaching the reactional system, determined by chemical actinometry); (iv) feed composition (in terms of $[H_2]:[CO_2]$ molar ratio); (v) temperature (under dark and light conditions); and (vi) photocatalyst reuse (for up to 10 cycles). Additionally, this work also intended to address the literature gap regarding the systematic understanding of how reaction products contribute to catalyst deactivation. The main findings of this research hold the potential to advance the knowledge of thermo-photocatalytic CO_2 methanation powered by sunlight at temperatures lower than those found in conventional methanation technologies.

2. Materials and methods

2.1. Chemical products

The chemical products (analytical grade) used throughout the experimental activities are briefly described in Table 1. All of them were used as received without further purification. Ultrapure water (UPW) used to prepare/wash the photocatalytic materials was produced by a Millipore Direct-Q® ultrapure-water system (resistivity of $18.2 \text{ M}\Omega \text{ cm}^{-1}$ at 25 °C).

Table 1

Description of the chemical products employed in the experiments.

Chemical product	Molecular formula	Concentration (wt%)	Density (kg L ⁻¹)	Molecular weight (g mol ⁻¹)	Supplier	Purpose
Pluronic P-123 or PEG-PPG-PEG ^a	(C ₃ H ₆ O.C ₂ H ₄ O) _x	97	—	average Mn ~5800	Sigma Aldrich	Preparation of the SBA-15 support
Tetraethoxysilane (TEOS)	SiC ₈ H ₂₀ O ₄	98	0.94	208.33		
Isopropanol	C ₃ H ₈ O		0.79	60.1	J.T. Baker	Functionalisation of the SBA-15 support with TiO ₂
Titanium isopropoxide	C ₁₂ H ₂₈ O ₄ Ti	97	0.96	284.22	Sigma Aldrich	
Ethylene glycol	C ₂ H ₆ O ₂	99.9	1.11	62.07	VWR chemicals international	Impregnation of RuO ₂ in the TiO ₂ /SBA-15 material
Ruthenium (III) chloride hydrate	RuCl ₃ ·H ₂ O		3.11	207.43	Merck	
Ethanol	C ₂ H ₅ OH	99.9	0.79	46.07	J.T. Baker	Washing of the catalytic materials
Acetone	C ₃ H ₆ O	99.5	0.78	58.08	JMGS	
Hydrochloric acid	HCl	37	1.18	36.46	Fisher Scientific	Digestion of the catalytic material samples to undergo ICP and FAAS analysis
Nitric acid	HNO ₃	65	1.51	63.01		
Hydrogen peroxide	H ₂ O ₂	30	1.45	34.01	Merck	
Hydrofluoric acid	HF	38	1.13	20.00		
ICP multi-elemental solution (in 15 % HCl)	Ir, Pt, Os, Rh, Pd, Ru	10 mg L ⁻¹	—	—	VWR	Standard solutions for ICP and FAAS calibration
Titanium standard solution (in 0.24 % F ⁻)	Ti	999 ± 3 µg L ⁻¹	—	—	SCP Science	
Potassium chloride	KCl	99.5	1.98	74.55	Scharlau	Ionization suppressor for FAAS analysis
Ferric chloride hexahydrate	Cl ₃ FeH ₁₂ O ₆	98	1.82	270.29	Merck	Actinometric tests
Oxalic acid dihydrate	C ₂ H ₆ O ₆	98	1.65	126.07	VWR chemicals international	
1,10-phenanthroline 1-hydrate	C ₁₂ H ₈ N ₂ ·H ₂ O	—	—	198.23	Panreac	Iron determination during actinometric tests
Acetic acid	CH ₃ COOH	100	1.05	60.05	Fisher	
Ammonium acetate	NH ₄ C ₂ H ₃ O ₂	—	—	77.08	Fisher	
L-ascorbic acid	C ₆ H ₈ O ₆	—	—	176.12	Acrós	
Carbon dioxide	CO ₂	99.998	1.87 × 10 ⁻³	44.01	Air Liquide	Gases for (i) methanation reaction (CO ₂ ; H ₂), (ii) GC-µTCD/FID analysis (H ₂ ; He; synthetic air), and (iii) GC-µTCD/FID equipment calibration (CO ₂ ; H ₂ ; CH ₄ ; C ₂ H ₆)
Hydrogen	H ₂	99.999	8.38 × 10 ⁻⁵	1.00		
Helium	He	99.999	1.79 × 10 ⁻⁴	4.00		
Synthetic air ^b	N ₂ + O ₂ (20 % ± 1 %)	99.999	—	—		
Methane	CH ₄	>99.5	6.57 × 10 ⁻⁴	16.04		
Ethane	C ₂ H ₆	>99.95	3.77 × 10 ⁻⁴	30.07		

^a Poly(ethylene glycol)-block-poly(propylene glycol)-block-poly(ethylene glycol);^b Impurities: H₂O: <3 ppm; C_nH_m: <0.1 ppm; CO₂: <1 ppm; CO: <1 ppm.

2.2. Preparation of the supported catalytic materials

2.2.1. Synthesis of mesoporous silica SBA-15

The SBA-15 support was synthesized under hydrothermal conditions, according to the experimental procedure reported in the literature [18–20] (Fig. 1a). Concisely, 4.1 g of Pluronic P123 triblock polymer was dissolved in 30 mL of UPW under stirring for 2 h at 35 °C. Then, 120 g of a hydrochloric acid (HCl) solution (2 mol L⁻¹) was added, keeping the resulting solution under agitation for 2 h more. Subsequently, 8.5 g (41 mmol) of tetraethoxysilane (TEOS) was slowly added to the solution and mixed for 24 h. Afterward, the mixture was hydrothermally synthesised on a Teflon autoclave bottle for 24 h at 100 °C. The product was collected by filtration, washed with 2 L of UPW and 250 mL of ethanol, and dried under airflow at room temperature overnight. The surfactant was extracted with ethanol in a Soxhlet extractor for 36 h. The resulting SBA-15 powder was oven-dried at 150 °C.

2.2.2. Functionalisation of SBA-15 support with TiO₂ semiconductor

After synthesising the SBA-15 support, TiO₂ was incorporated into it by the sol-gel method [21] (Fig. 1b). In summary, 1 g of SBA-15 was suspended in 10 mL of isopropanol by sonication (Vibra Cell™VCX 130, Sonics, Newtown, USA) for 30 min at 20 kHz (80 % amplitude; pulse 1-on and 2-off). Subsequently, different volumes of titanium isopropoxide (TTIP) were added to the colloidal suspension (see Table S1) to

attain [TiO₂]:[SBA-15] mass ratios of 1:10, 2:10 and 3:10 and kept under stirring for 45 min. In sequence, UPW was introduced into the mixture (with a TTIP:H₂O volume ratio of 1:10), and stirring was maintained until complete TTIP hydrolysis. The resulting material was recovered by vacuum filtration (Nylon membrane filter, 0.22 µm, Ø 47 mm), washed with UPW and ethanol, and slowly dried in an oven for 2 days at 100 °C. Finally, the resulting powder was calcinated for 2 h at 700 °C to form TiO₂ crystals on the SBA-15 surface (TiO₂/SBA-15). The actual titanium (Ti) concentration supported on SBA-15 for each photocatalyst composition was estimated by flame atomic absorption spectrometry (FAAS), whose values are depicted in Table S1.

2.2.3. Impregnation of RuO₂ metal oxide in the TiO₂/SBA-15 nanocomposite

The RuO₂ was impregnated in the TiO₂/SBA-15 composite by ethylene glycol-mediated synthesis (Fig. 1c), similar to the method reported in a previous work [22]. In a nutshell, different amounts of ruthenium (III) chloride hydrate (RuCl₃·H₂O) (see Table S1) were added to a suspension of TiO₂/SBA-15 powder in ethylene glycol (5 mg mL⁻¹, 25 mL), previously obtained by sonication for 30 min at 20 kHz (80 % amplitude, pulse 1-on 2-off), to attain [Ru]:[TiO₂/SBA-15] mass ratios of 0.4:10, 0.8:10, 1.2:10, 1.6:10 and 2.0:10. Then, the suspension underwent heating for 5 h at 100 °C, followed by refluxing for 8 h at 180 °C, under continuous stirring (500 rpm). In sequence, the solid sample

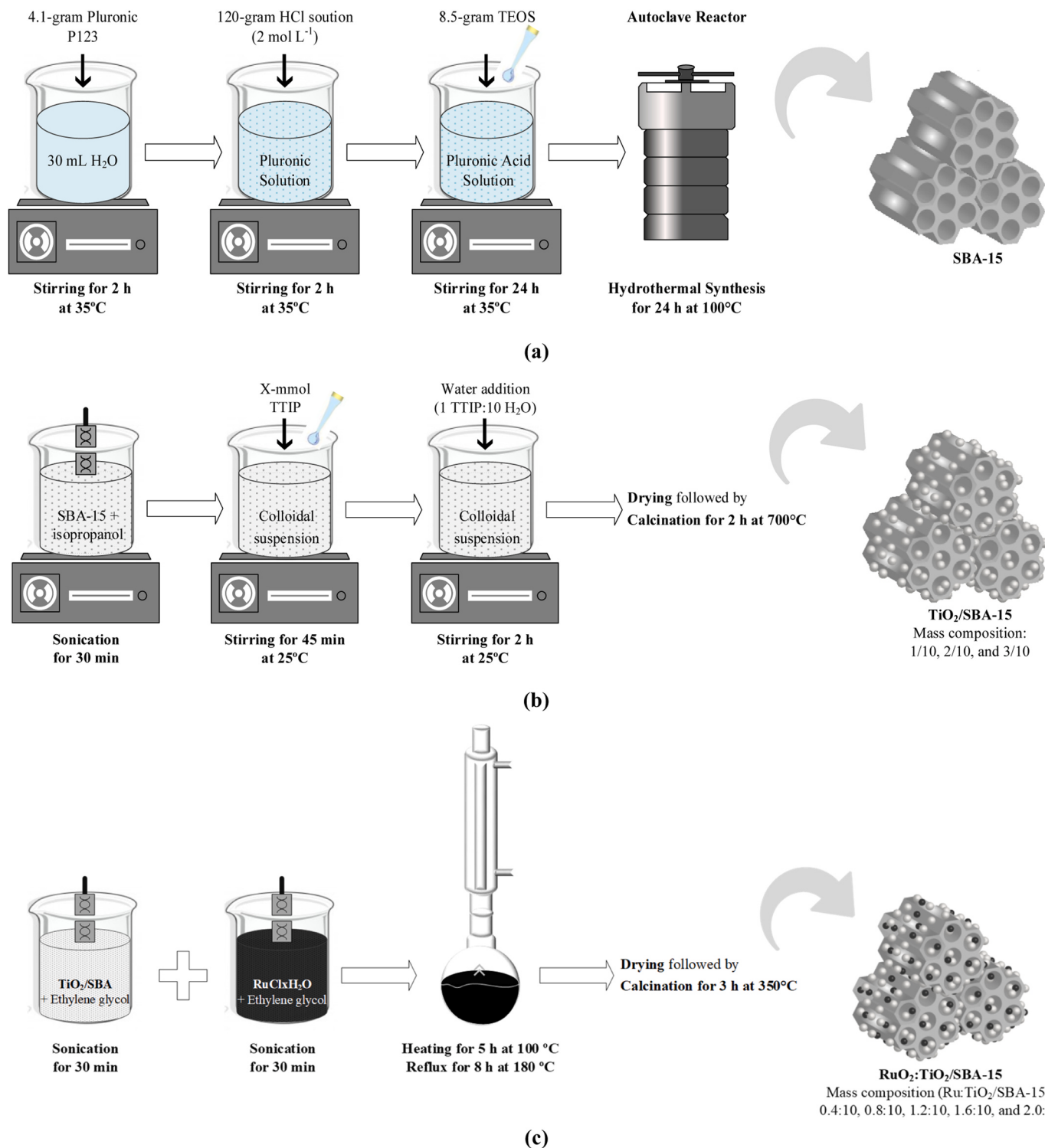


Fig. 1. Sequential preparation methodology of the hybrid RuO₂:TiO₂/SBA-15 photocatalyst: (a) synthesis of mesoporous silica SBA-15 support; (b) functionalisation of SBA-15 support with TiO₂ semiconductor; (c) impregnation of RuO₂ into the TiO₂/SBA-15 nanocomposite.

was separated by filtration (Nylon membrane filter, 0.22 µm, Ø 47 mm), washed with 1 L of UPW and 200 mL of acetone, and dried for 1 h at 100 °C. Lastly, the resulting powder was oxidised by calcination for 3 h at 350 °C (Nabertherm Furnace, Germany) under an ambient atmosphere. The actual ruthenium (Ru) concentration in the catalytic material was determined by inductively coupled plasma emission spectrometry (ICP-OES), whose values are displayed in Table S1. The resulting photocatalyst was kept inside a desiccator until use to avoid humidity

interference.

2.3. Materials characterisation techniques

All analytical techniques employed in the characterisation of the synthesised materials are described in the Supplementary Material file (Table S2).

2.4. Experimental procedure

The materials' catalytic activity towards photo-assisted CO₂ methanation was evaluated in a batch-mode thermo-photocatalytic system (Fig. 2) under the gas-phase. The experimental apparatus encompassed: (i) a 40 mL cylindrical quartz photoreactor; connected to (ii) a feeding system, composed of H₂/CO₂ gas bottles and Swagelok (Ohio, USA) connections (tubing, fittings and valves); (iii) a pressure control system (up to 4 bar), to regulate the reactor pressure/reactants feeding; (iv) a temperature controlling system (up to 300 °C), composed of a fibreglass heating ribbon (FHR), surrounding the reactor, coupled to a digital thermostat temperature controller (DTTC); (v) an irradiation source, which could be a xenon (Xe) lamp equipped in a sunlight simulator (Atlas, Suntest XLS⁺, Linsengericht, Germany), emitting polychromatic radiation between 280 and 800 nm (Fig. S1), or a light emitting diode (LED), emitting monochromatic radiation at 365 nm or 405 nm; and (vi) an *on-line* gas chromatography (GC) analytical system (YL 6500, YL Instrument CO. LTD, Anyang, Korea) to analyse the gas samples directly withdrawn from the reactor headspace by means of a peristaltic pump. It is worth mentioning that the internal reactor temperature and catalyst surface temperature were confirmed with a digital infrared thermometer (UNIT-T, UT300S) when required.

In order to allow online detection/quantification of the reactants and products at the same time, the GC analytical system is composed of (i) two columns in series, (1) a Carbon Plot column ($30\text{ m} \times 0.32\text{ mm} \times 3.0\text{ }\mu\text{m}$, Agilent Technologies, California, USA), to separate CO_2 and C_2H_6 , and (2) a Mol Sieve 5 A Plot fused silica capillary column ($30\text{ m} \times 0.32\text{ mm} \times 3.0\text{ }\mu\text{m}$, Supelco, Missouri, USA), to separate H_2 and CH_4 ; (ii) two detectors, (1) a micro-thermal conductivity detector (μTCD), with the sensitivity of 400 pg mL^{-1} , for H_2 quantification, followed by (2) a flame ionisation detector (FID), with sensitivity $1.5\text{ pg carbon sec}^{-1}$, for CO_2 , CH_4 , and ethane (C_2H_6) quantification; and (iii)

one methaniser, placed between the μ TCD and FID, to convert CO_2 into CH_4 . The GC has two six-way valves: (i) a primary injecting valve, placed before the first column, which allows online products' analysis (through the sampling loop) and ensures that a consistent gas volume is injected into the columns; and (ii) a second switching valve, placed between the two columns, which directs gas flow from the Carbon Plot column to the detectors, bypassing the Molsieve 5 Å column, protecting it from high concentrations of CO_2 and C_{2+} elements, thus reducing the need for frequent column regeneration [23]. The molar composition of the gas mixture inside the photoreactor was estimated by area normalisation with response factors.

The thermo-photocatalytic methanation experiments proceeded as follows: (i) firstly, the composite photocatalyst ($\text{TiO}_2/\text{SBA-15}$; $\text{RuO}_2/\text{SBA-15}$ or $\text{RuO}_2\text{-TiO}_2/\text{SBA-15}$) was added to the quartz reactor (10, 20, or 30 mg) followed by 10 min purge with H_2 flux; (ii) then, the mixture of H_2 and CO_2 were fed to the reactor ([CO_2]:[H_2] molar ratio of 1:2, 1:4, or 1:7) by pressure control ($P_{\text{CO}_2}:P_{\text{H}_2}$ (bar/bar) of 0.32:0.64, 0.32:1.28, or 0.32:2.24); (iii) before starting the reaction, the first sample was taken at ambient temperature after 20-min stabilization and leaks checking; iv) sequentially, the heating system was switched on (50, 100, 150, 200, or 250 °C), and the second sample was collected after a 10-min stabilization period under dark conditions; (v) right after, the illumination source was turned on (radian power (RP) of (1) 0.211 ± 0.004 , 0.339 ± 0.006 , 0.45 ± 0.01 or 1.09 ± 0.03 W, for Xe lamp, (2) 0.053 ± 0.009 , 0.17 ± 0.03 , 0.30 ± 0.05 , or 0.55 ± 0.08 W, for LED at 365 nm, or (3) 0.055 ± 0.008 , 0.18 ± 0.02 , 0.37 ± 0.06 or 0.55 ± 0.07 W, for LED at 405 nm, determined by ferrioxalate actinometry as described in Section 2.5.3); and (vi) four more samples were gathered up to 110 min reaction. After the reaction, the reactor was cooled down and cleaned with a compressed air jet, followed by UPW rinsing and drying for 3 h at 100 °C.

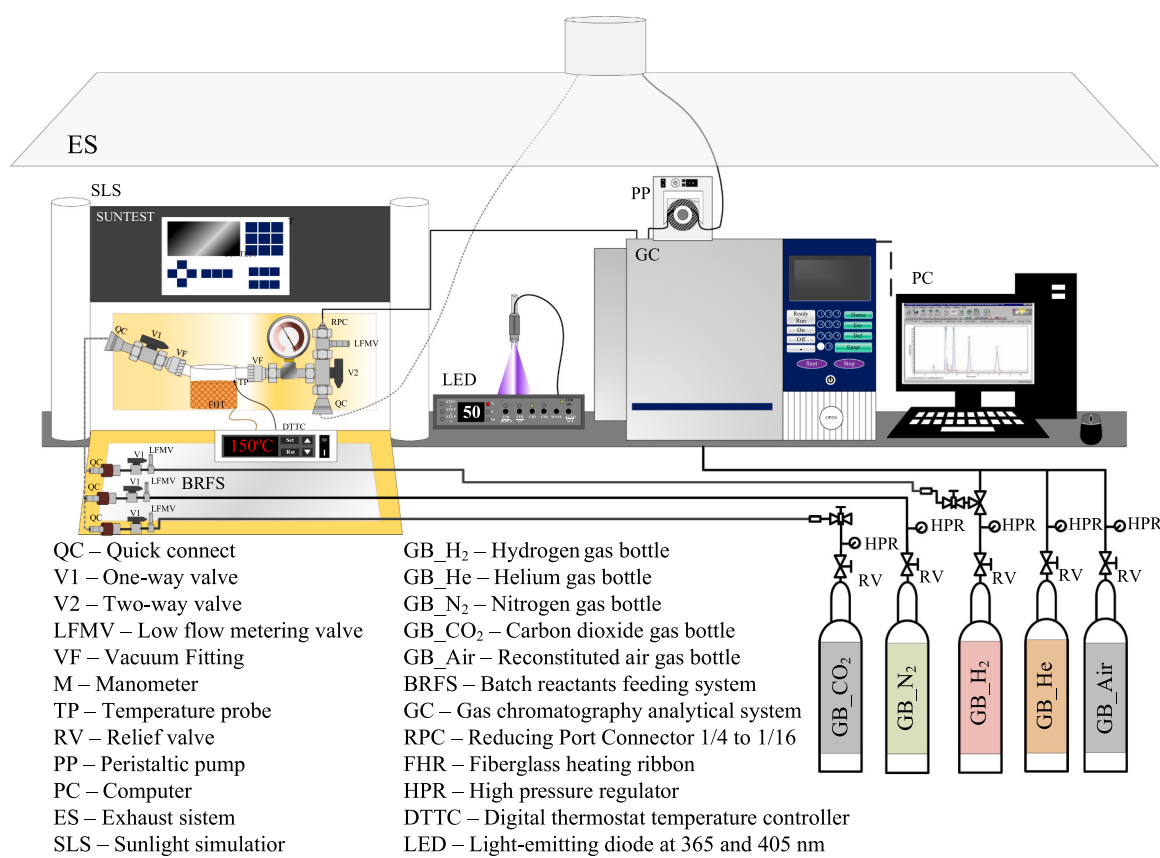


Fig. 2. Sketch of the batch-mode gas-phase thermo-photocatalytic methanation system.

2.5. Calculation formulas

2.5.1. CO₂ reduction efficiency

The efficiency of the CO₂ reduction reaction was assessed through the percentage of CO₂ reactant converted (X_{CO_2}), product yield (Y_{CH_4} and $Y_{C_2H_6}$), and product selectivity (S_{CH_4} and $S_{C_2H_6}$), according to Eqs. (1) to (5) [6].

$$X_{CO_2} (\%) = \left(1 - \frac{[CO_2]_f}{[CO_2]_0} \right) \times 100 \quad (1)$$

$$Y_{CH_4} (\%) = \left(\frac{[CH_4]_f}{[CO_2]_0} \right) \times 100 \quad (2)$$

$$Y_{C_2H_6} (\%) = \left(\frac{2 \times [C_2H_6]_f}{[CO_2]_0} \right) \times 100 \quad (3)$$

$$S_{CH_4} (\%) = \frac{Y_{CH_4}}{X_{CO_2}} \times 100 \quad (4)$$

$$S_{C_2H_6} (\%) = \frac{Y_{C_2H_6}}{X_{CO_2}} \times 100 \quad (5)$$

X_{CO_2} was estimated by the relation between its final (at 110 min reaction) and initial molar concentration ([CO₂]_f and [CO₂]₀, respectively) (Eq. (1)). Y_{CH_4} and $Y_{C_2H_6}$ were given by the ratio of the actual final molar concentrations (at 110 min reaction) of CH₄ and C₂H₆ ([CH₄]_f and [C₂H₆]_f, respectively) over the [CO₂]₀, which is the theoretical CO₂ concentration that could fully have been converted into CH₄ or C₂H₆ products (Eqs. (2) and (3), respectively). S_{CH_4} and $S_{C_2H_6}$ were determined from the ratio between the Y_{CH_4} and $Y_{C_2H_6}$, respectively, and the X_{CO_2} (Eqs. (4) and (5), respectively).

The pseudo-first-order kinetic constant for CO₂ reduction (k_{CO_2} or k'_{CO_2} , in min⁻¹ or L kJ⁻¹) was estimated by non-linear regression (Fig.P software of Biosoft) from Eqs. (6) and (7), as a function of time (t , in min) or accumulated energy (Q , in kJ L⁻¹), respectively. In turn, the Q was obtained from the radiant power (RP , in J s⁻¹) reaching inside the reactor, reaction time (t , in s), and reactor volume (V , in L), as depicted in Eq. (8). Also, initial CO₂ reduction rate (r_0 , in mmol L⁻¹ min⁻¹) was calculated through Eq. (9).

$$[CO_2]_t = [CO_2]_0 \times \exp^{-k_{CO_2} \times t} \quad (6)$$

$$[CO_2]_Q = [CO_2]_0 \times \exp^{-k'_{CO_2} \times Q} \quad (7)$$

$$Q = \frac{RP \times t}{1000 \times V} \quad (8)$$

$$r_0 = [CO_2]_0 \times k_{CO_2} \quad (9)$$

where the [CO₂]_t and [CO₂]_Q stand for CO₂ molar concentration (in mmol L⁻¹) at time t and accumulated energy Q .

2.5.2. Apparent photonic efficiency and apparent quantum yield

The photon-to-CO₂ conversion efficiency was evaluated by the: (i) apparent photonic efficiency ($\Phi_{CO_2}^{APE}$), taking into account the number of CO₂ mol converted per second ($r_0 \times V$, in mol s⁻¹) and the photon flux (Pa_λ , in Einstein s⁻¹, with $\lambda = 365/405$ nm for LEDs illumination and $\lambda = 280-800$ nm for simulated solar light, section 2.5.3) reaching inside the reactor, in line with Eq. (10) [24]; and (ii) apparent quantum yield ($\Phi_{CO_2}^{AQY}$), further considering the apparent fraction of light absorbed by the photocatalyst (f , section 2.5.4), as displayed in Eq. (11).

$$\Phi_{CO_2}^{APE} = \frac{r_0 \times V}{Pa_\lambda} \times 100 \quad (10)$$

$$\Phi_{CO_2}^{AQY} = \frac{r_0 \times V}{Pa_\lambda \times f} \times 100 = \frac{\Phi_{CO_2}^{APE}}{f} \quad (11)$$

2.5.3. Photon flux

Most studies determine the number of incident photons through the lamp's useful power divided by the average photon energy. This does not ensure experimental accuracy, especially when dealing with polychromatic illumination. In this sense, actual Pa_λ striking the photocatalyst surface, either under monochromatic irradiation (365 and 405 nm) or polychromatic one (between 280 and 800 nm), was estimated by ferrioxalate actinometry ([Fe³⁺] = 23 mM; [Fe³⁺]:[oxalic acid] molar ratio of 1:5; $V = 40$ mL; sampling timeframe of 30 s; test ended at 25 % of ferrioxalate degradation), which is suitable for UV-Vis measurements up to 580 nm (see Fig. S1), as reported elsewhere [25, 26]. The photochemical conversion of ferric ions (Fe³⁺) into ferrous ions (Fe²⁺) was quantified by the formation of the coloured tris-phenanthroline complex ($\epsilon = 11100$ L mol⁻¹ cm⁻¹ at $\lambda_{max} = 510$ nm), according to ISO 6332:1988 method. First, the radiant power (RP_λ , in J s⁻¹) emitted by the illumination source that reached the internal reactor wall was determined from Eq. (12); Then, Pa_λ (Einstein s⁻¹) was calculated from Eq. (13), adapted from Bossmann et al. [25].

$$RP_\lambda = \frac{dn(Fe^{2+})}{dt} \times \frac{N_A}{\sum_{\lambda_f}^{\lambda_i} \left[\frac{S_{e,\lambda}}{E_{ph,\lambda}} \times (1 - 10^{-A_\lambda}) \times \Phi_\lambda \right]} \quad (12)$$

$$Pa_\lambda = RP_\lambda \times \sum_{\lambda_i}^{\lambda_f} \left[\frac{S_{e,\lambda}}{E_{ph,\lambda}} \times (1 - 10^{-A_\lambda}) \right] \quad (13)$$

where: $dn(Fe^{2+})/dt$ (mol s⁻¹) is the number of Fe²⁺ mol formed per irradiation time; N_A is the Avogadro number (6.02×10^{23} mol⁻¹); $S_{e,\lambda}$ is the relative spectral distribution of the illumination source (estimated through the integration of the Xe lamp spectral irradiance (Fig. S1), between 280 and 580 nm, for polychromatic irradiation, and equal to one for monochromatic irradiation); $E_{ph,\lambda}$ (J) is the photon energy at a wavelength λ (Eq. (14)); A_λ is average absorbance of the ferrioxalate solution at a wavelength λ (Eq. (15)), considering the irradiation timeframe, and Φ_λ is the quantum yield of the ferrioxalate actinometer at a wavelength λ (Fig. S1).

$$E_{ph,\lambda} = \frac{h \times c}{\lambda} \quad (14)$$

$$A_\lambda = \epsilon_\lambda \times b \times C \quad (15)$$

where: h is the Planck's constant (6.63×10^{-34} J s⁻¹); c is the light velocity (3.00×10^8 m s⁻¹); ϵ_λ is the molar absorptivity of the ferrioxalate solution at a wavelength λ (L mol⁻¹ cm⁻¹); b is photoreactor light path length (cm); and C is the average concentration of the ferrioxalate solution (mol L⁻¹), during the irradiation timeframe.

As regards the polychromatic illumination source, it should be noted that RP and Pa were quantified from actinometry only between 280 nm, the lower limit of the Suntest's Xe lamp, and 580 nm (RP₂₈₀₋₅₈₀ and Pa₂₈₀₋₅₈₀), the upper limit of ferrioxalate absorption. To estimate the values of both parameters for the total Suntest spectrum, that is, between 280 and 800 nm (RP₂₈₀₋₈₀₀ and Pa₂₈₀₋₈₀₀), the upper limit of the Xe lamp, Eqs. (16) and (17) were applied, taking into account the integration of the spectral irradiance (E , in J s⁻¹ m⁻² nm⁻¹) and spectral photon irradiance (E_p , in Einstein s⁻¹ m⁻² nm⁻¹) of the Suntest's Xe lamp (Fig. S1).

$$RP_{280-800} = \frac{\int_{280}^{800} (E) d\lambda}{\int_{280}^{580} (E) d\lambda} \times RP_{280-580} \quad (16)$$

$$Pa_{280-800} = \frac{\int_{280}^{800} (E_p) d\lambda}{\int_{280}^{580} (E_p) d\lambda} \times Pa_{280-580} \quad (17)$$

2.5.4. Fraction of light absorbed by the photocatalyst

If the reactor is under the same conditions as the UV-Vis DRS analysis, the apparent fraction of the photons absorbed by the photocatalyst can be estimated using the Kubelka-Munk (K-M) equation (Eq. (18)) [27]. Under batch-mode and gas-phase operating conditions, the scattered and reflected light effects are similar to UV-Vis DRS measurement [24,28]. So, the (average) apparent fraction of light absorbed by the photocatalyst (f), for absorbance ≥ 0.05 , can be estimated by the absolute reflectance of the material through the K-M function ($F(R_\infty)$), as described in Eq. (19) and Eq. (20), if considering monochromatic and polychromatic illumination sources, respectively.

$$F(R_\infty)(\lambda) = \frac{(1 - R_\infty)^2}{2 \times R_\infty} = \frac{K}{S} \quad (18)$$

$$f_\lambda = F(R_\infty)(\lambda) \times S \quad (19)$$

$$f_{\lambda_f - \lambda_i} = \frac{\int_{\lambda_i}^{\lambda_f} (F(R_\infty)(\lambda) \times S) d\lambda}{\lambda_f - \lambda_i} \quad (20)$$

where, R_∞ is the absolute reflectance, with the subscript ∞ denoting a sample layer thickness high enough to entirely hide the support, K and S are the K-M absorption and scattering coefficients, respectively, f_λ is the

apparent fraction of monochromatic light absorbed by the photocatalyst for the wavelength λ (with $\lambda = 365/405$ nm for UV/Vis LEDs), and $f_{\lambda_f - \lambda_i}$ is the average apparent fraction of polychromatic light absorbed by the photocatalyst across a wavelength interval (with $\lambda_i = 280$ nm and $\lambda_f = 800$ nm for simulated sunlight).

2.5.5. Activation energy for CO₂ reduction

The apparent activation energy (E_a , in J mol⁻¹) for CO₂ reduction was estimated by non-linear regression (Fig.P software of Biosoft) from the Arrhenius equation (Eq. (21)).

$$k_{CO_2} = A e^{-\frac{E_a}{RT}} \quad (21)$$

Where, k_{CO_2} is the time-based pseudo-first-order kinetic constant for CO₂ reduction, A is frequency factor, R is the universal gas constant ($R = 8.314$ J mol⁻¹ K⁻¹) and T is the absolute temperature (in K⁻¹).

3. Results and discussion

3.1. Materials characterisation

The structural, morphological, and textural characteristics of the RuO₂:TiO₂/SBA-15 nanocomposite photocatalyst featuring the best composition were analysed by: (i) Fourier Transform Infrared (FTIR)

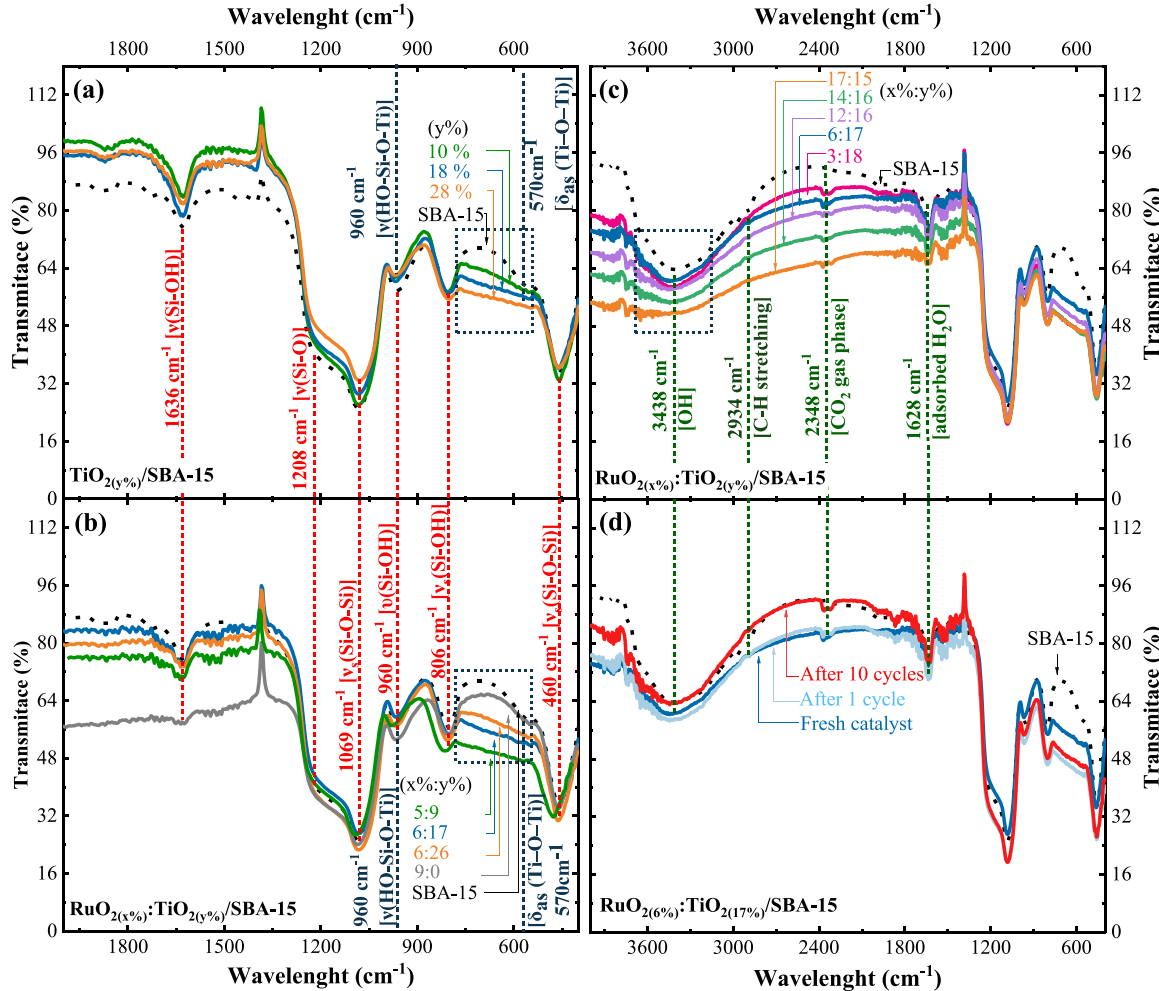


Fig. 3. FTIR spectra of the pristine SBA-15 support (dashed line) and hybrid photocatalysts (solid line) for different experiments sets: (a) influence of the TiO₂ load on SBA-15 in the absence of RuO₂ (TiO₂(y%)/SBA-15, with $y = 10, 18$, and 28 wt%); (b) influence of the TiO₂ load on the SBA-15 in the presence of RuO₂, keeping [Ru]:[TiO₂/SBA-15] mass ratio at $0.8:10$ (RuO₂(x%):TiO₂(y%)/SBA-15, with $x\%:y\% = 9:0, 5:9, 6:17$, and $6:26$); (c) influence of the RuO₂ load on the TiO₂/SBA-15, keeping [TiO₂]:[SBA-15] mass ratio at $2:10$ (RuO₂(y%):TiO₂(x%)/SBA-15, with $x\%:y\% = 3:18, 6:17, 12:16, 14:16$, and $17:15$); and (d) influence of the photocatalytic material reuse (RuO_{2(6.4%)}:TiO_{2(16.9%)}/SBA-15 fresh and after 1 and 10 utilization cycles under the best operating conditions).

spectroscopy (Fig. 3); (ii) Scanning Electron Microscopy (SEM) and Energy Dispersive X-ray Spectroscopy (EDS), and EDS elemental mapping and Transition Electron Microscopy (TEM) (Fig. 4); (iii) Brunauer–Emmett–Teller (BET) theory (Table S3); (iv) UV-vis Diffuse Reflectance Spectroscopy (DRS) (Fig. 5); (v) X-ray Powder Diffraction (XRD) (Fig. 6); and X-Ray Photoelectron Spectroscopy (XPS) (Fig. 7). Additionally, FTIR (for all material compositions), SEM-EDS, DRS, and XRD techniques were used to characterise SBA-15 and TiO₂/SBA-15 samples. FTIR and XPS were also employed to analyse the hybrid RuO₂:TiO₂/SBA-15 composite after 1/10 and 10 thermo-photocatalytic cycles, respectively.

3.1.1. FTIR spectroscopy

Fig. 3 depicts the FTIR spectra for all samples: SBA-15, SBA-15 incorporated with TiO₂, and RuO₂ impregnated in the TiO₂/SBA-15 composite. Six infrared (IR) active vibration modes caused by Si-O bonds or Si-OH groups were detected in the mesoporous silica spectra at 400–2000 cm⁻¹ (the red highlights in Fig. 3a–b). Due to the twisting motion in the tetrahedral [₃OSi-O-SiO₃] cluster, the first IR activation mode at about 460 cm⁻¹ is related to the symmetrical bending vibration of the ν(Si-O) bond [29,30]. The symmetric stretching vibration of the (Si-OH) bond in the silanol group results in the IR active modes at 960 and 806 cm⁻¹ [31,32]. Additionally, the band at 1082 cm⁻¹ is caused by the antisymmetric tensile vibration of the ν(Si-O) bond in the [Si-O₄] cluster. Also, the shoulder at 1208 cm⁻¹ represents the antisymmetric tensile vibration of the ν(Si O) bond. Lastly, the absorption band at 1636 cm⁻¹ can be caused by water adsorbed on the SBA-15 surface, representing the bend vibration of the ν(Si-OH) bond [29,30].

SBA-15 functionalization with semiconductor results in a low-strength band at 570 cm⁻¹ relating to stretching δ as (Ti-O-Ti) of TiO₂ [31]. The rise in TiO₂ amount supported in mesoporous silica is correlated to the reduction in transmittance at 570 cm⁻¹. As previously mentioned, the band at 960 cm⁻¹ represents the presence of Si-OH groups; nevertheless, this peak can also represent the asymmetric Si-O-Ti vibration in the molecular sieve that contains titanium in the composed material [33] (Fig. 3a–c).

According to Natarajan and Basu [34] and Joshi and Sutrave [35], the characteristic bands around 474, 530, 880, and 750 cm⁻¹ represent

the stretching mode of Ru-O, Ru–O–Ru, Ru=O, and O–Ru–O, respectively. However, these bands were not detected in the RuO_{2(y%)}:TiO_{2(x%)}/SBA-15 photocatalyst due to its complex structure (where y and x are the weight percentages of RuO₂ and TiO₂, respectively). In this case, RuO₂-loaded was evidenced by a large band between 3000 cm⁻¹ and 3757 cm⁻¹, which provides stretching vibrations of -OH, confirming the formation of hydrated metal oxide [35,36] (Fig. 3b–c).

Furthermore, the FTIR analysis also identifies some components that can easily be adsorbed on the mesoporous catalyst (Fig. 3d): (i) water at 1628 and 3438 cm⁻¹ with -OH band, (ii) gaseous CO₂ band at 2348 cm⁻¹, and (iii) C–H stretching vibration that appears at 2934 cm⁻¹ [32]. The peaks of the adsorbed components become more evident after the use of the catalyst. However, there are no relevant changes in the catalyst FTIR spectrum, after its first use. The main exception is the modifications between 3000 cm⁻¹ and 3757 cm⁻¹ after the 10th reuse cycle, which are related to the RuO₂, as further explored in XPS analysis (Section 3.2.6).

3.1.2. Morphology and textural characteristics

Fig. 4a shows the morphological behaviour of the material according to its composition by SEM/EDS analysis. SEM images of mesoporous silica (Fig. 4a.1) exhibit morphology analogous to uniform cylindrical long-rod particles, in agreement with results found in the literature for SBA-15 [37]. SBA-15 functionalised with TiO₂ (Fig. 4a.2, TiO₂ (18.2%)/SBA-15) showed an uneven distribution of TiO₂ over the SBA-15 structure (Fig. 4a.3), while retaining the mesoporosity features of the SBA-15. This configuration enhances mass photon transfer, adsorption and light scattering between the material layers [14]. As expected, EDS (Fig. 4a) and TEM mapping (Fig. 4b) confirm the presence of all the elements used in the photocatalyst preparation steps, such as Si, O, Ti, and Ru, as well as the absence of any impurity.

Fig. 4c shows the TEM images of the RuO_{2(6.4%)}:TiO_{2(16.9%)}/SBA-15 sample in different magnitudes. Remarkably, the TEM image reveals the preservation of the 2D hexagonal structure of the mesoporous silica, highlighting the material's structural integrity [37]. In addition, the distribution of RuO₂:TiO₂ nanoparticles on the surface of the SBA-15 material can be observed, showing a well-dispersed arrangement of these nanoparticles. This characterisation confirms the successful

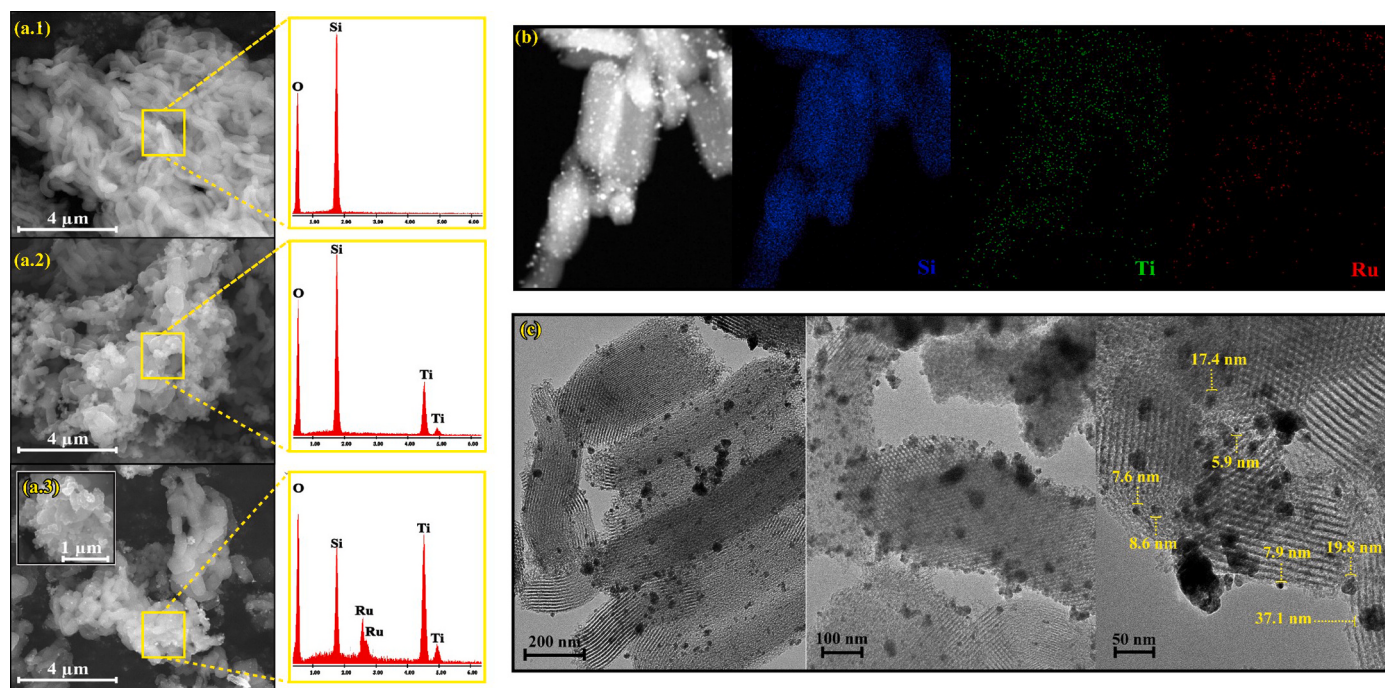


Fig. 4. SEM micrographs and EDS spectra for (a.1) SBA-15, (a.2) TiO₂(18.2%)/SBA-15, (a.3) RuO₂(6.4%):TiO₂(16.9%)/SBA-15 materials, along with the (b) EDS elemental mapping (Si, Ti, Ru) and (c) TEM images for the RuO₂(6.4%):TiO₂(16.9%)/SBA-15 photocatalyst.

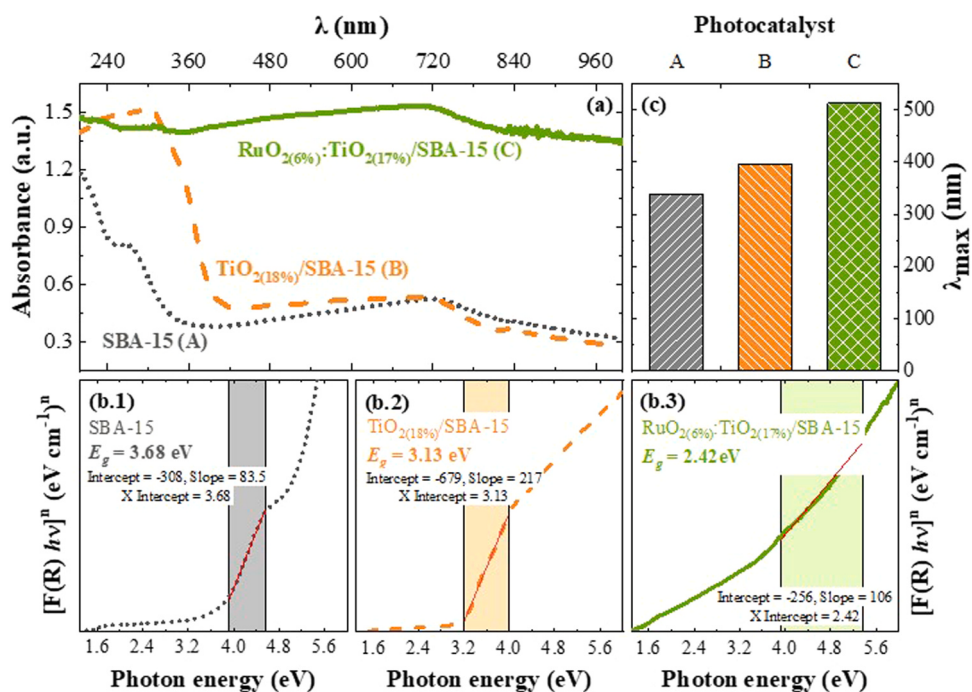


Fig. 5. Representation of the (a) UV-vis DRS data, (b) optical band gap energy (E_g) determination (Tauc Plot method) and (c) maximum wavelength (λ_{max}) for electrons excitation (estimated from E_g) for (.1) SBA-15 (A), (.2) TiO₂(18.2%)/SBA-15 (B), and (.3) RuO₂(6.4%):TiO₂(16.9%)/SBA-15 (C) materials.

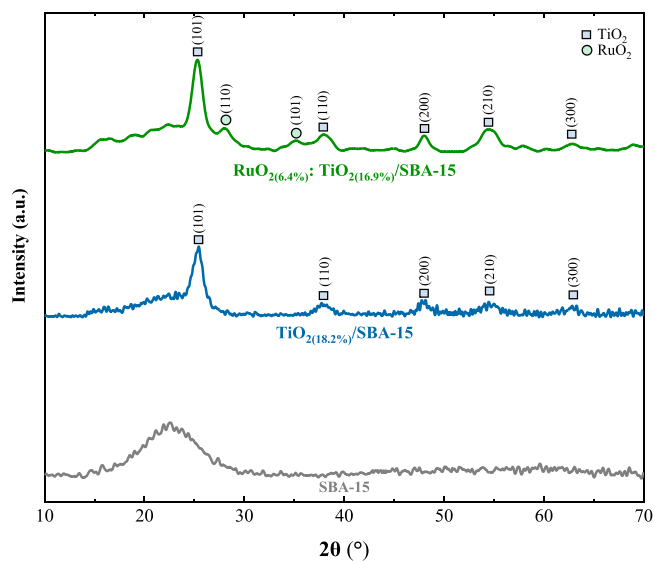


Fig. 6. XRD patterns for the SBA-15, TiO₂(18.2%)/SBA-15, and RuO₂(6.4%):TiO₂(16.9%)/SBA-15 materials.

incorporation of the RuO₂:TiO₂ catalyst onto the SBA-15 support, which is crucial for efficient catalytic processes and holds potential for various applications that require high surface area and controlled nanoparticle distribution. The largest particles with dimensions between 17.4 and 37.1 nm are related to TiO₂ functionalisation. According to Sahu et al. [38], the smaller TiO₂ nanoparticle size refers to the mesoporous confinement effect resulting in the inhibition of TiO₂ growth. Furthermore, no crystalline TiO₂ was observed. The smaller particles, ranging from 5.9 to 8.6 nm, can be attributed to the catalyst loading with RuO₂ [22].

The textural characteristics of pristine SBA-15, TiO₂(18.2%)/SBA-15, and RuO₂(6.4%):TiO₂(16.9%)/SBA-15 materials were reported in Table S3. Nitrogen adsorption-desorption isotherms were type IV with H1

hysteresis loops, corresponding to the mesoporous materials with two-dimensional hexagonal structures [39]. The mean pore diameter (D_{mean}) was between 2 and 50 nm and is classified by the International Union of Pure and Applied Chemistry (IUPAC) as mesoporous. The specific surface areas (S_{BET}) were higher than $440 \text{ m}^2 \text{ g}^{-1}$ for all samples tested, which was consistent with the type of material [20]. The functionalisation of SBA-15 with TiO₂ had a more impact on the textural characteristic's parameters due to the greater abundance and size of the TiO₂ particle than the deposited RuO₂ particle. The mesopore volume (V_{meso}) decreased from 1.05 to $0.84 \text{ cm}^3 \text{ g}^{-1}$ comparing the SBA-15 with RuO₂(6.4%):TiO₂(16.9%)/SBA-15 sample. The results show that some TiO₂ and RuO₂ have entered the SBA-15 mesopores [40]. The D_{mean} was 7.17, 6.24, and 6.41 for SBA-15, TiO₂(18.2%)/SBA-15, and RuO₂(6.4%):TiO₂(16.9%)/SBA-15, respectively. As the specific surface area, pore volume, and pore diameter of the composed material decreased compared to SBA-15, it can be implied that the TiO₂ and RuO₂ nanoparticles were also located inside the mesopores [20].

3.1.3. UV-vis diffuse reflectance spectra

Fig. 5 depicts the UV-Vis DRS spectra (Fig. 5a), with the bandgap determination by Tauc Plot [41] (Fig. 5b.1–3) and the maximum wavelength (λ_{max}) capable of triggering electronic excitation in the photocatalyst (Fig. 5c) for SBA-15, TiO₂(18.2%)/SBA-15, and RuO₂(6.4%):TiO₂(16.9%)/SBA-15. The SBA-15 functionalised with TiO₂ shows a high absorbance in the UV region (200–400 nm, Fig. 5a) with an optical band gap energy (E_g) of 3.13 eV (Fig. 5b.2), similar to commercial TiO₂ (3.2 eV). A blue shift of the semiconductor's bandgap can be related to the known quantum size effect for semiconductors caused by SBA-15 porous size restriction [42]. The silica-supported TiO₂ provides a broad absorption band representing (i) the titanium atoms in octahedral coordination for absorption between 290 and 330 nm and (ii) the presence of hydrated titanium in 232 nm favoured by the hydrophilic nature of the silica surface [43]. In addition, the incorporation of RuO₂ onto TiO₂/SBA-15 increased the plasmon band absorption [11,22], evidenced by strong, broad, and continuous spectrum-wide absorption in the UV (280–400 nm), visible (400–780 nm), and NIR (780–1000 nm) regions, which improves the overall solar conversion

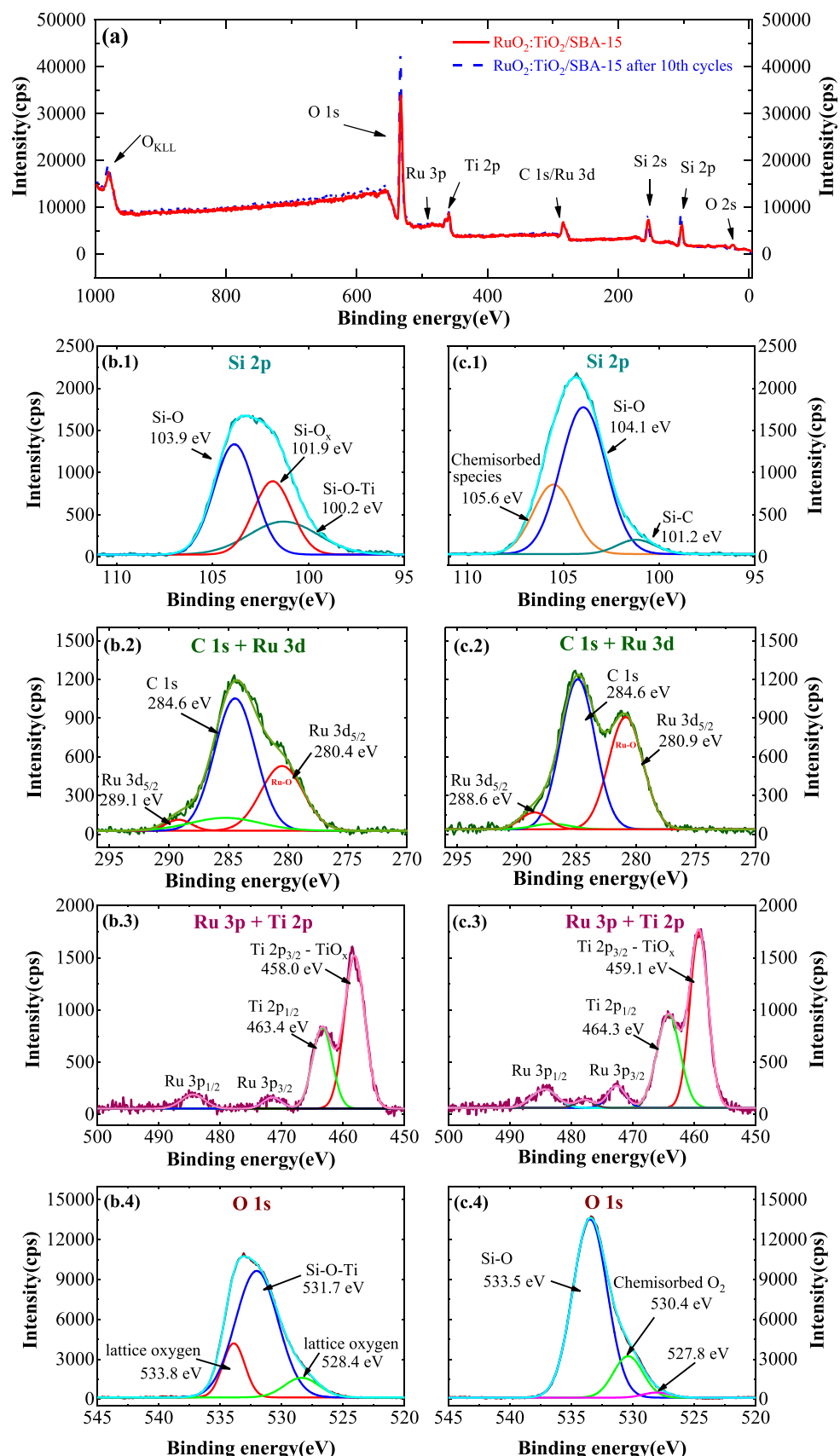


Fig. 7. Representation of the (a) overall XPS survey spectrum and high-resolution XPS spectra centered on the (.1) Si 2p, (.2) C 1 s + Ru 3d, (.3) Ru 3p + Ti 2p, (.4) O 1 s regions for the (b) fresh RuO_{2(6.4%)}:TiO_{2(16.9%)}/SBA-15 photocatalyst and (c) after 10 utilization cycles, along with the respective fitting and deconvolution curves.

efficiency. This extended absorption of Vis–NIR photons can promote several mechanisms, including: i) direct e–h pair generation, ii) indirect e–h pair generation, and iii) photothermal catalysis or thermal catalysis (i.e. plasmonic localized heating, non-radiative relaxation of semiconductors, and thermal vibration in molecules) where photons are converted into heat for promoting photo-redox catalysis [44]. Therefore, the lower bandgap energy of 2.42 eV (Fig. 5b,3) allows the absorption of photons at higher λ_{max} , enhancing the photo-response and photocatalytic efficiency.

To further corroborate the modification in the optical band gap energy, the Urbach energy (E_u) was also determined for $\text{TiO}_2(18.2\%)/\text{SBA-15}$ and $\text{RuO}_{2(6.4\%)}\text{-TiO}_2(16.9\%)/\text{SBA-15}$ samples (Fig. S2). The width of the defect bands caused by atomic structural disorder affects the optical transitions between the valence and conduction bands, resulting in localised states in the band tails, which is known as the Urbach tail. The energy associated with these defect states is referred to as Urbach energy (E_u), serving as a valuable parameter to assess the existence of tail-like energy levels within the bandgap. Such defects can be generated during the growth process, creating lattice disorder and stress in the material [45,46]. When RuO_2 was loaded into $\text{TiO}_2/\text{SBA-15}$, the E_u increased from 0.5 to 2.4 eV, indicating the formation of bad gap defects. This behaviour also suggests that the $\text{RuO}_{2(6.4\%)}\text{-TiO}_2(16.9\%)/\text{SBA-15}$ nanoparticle has a broader tailing and higher atomic structural disorder, which reduces the E_g , allowing the transition of electrons even under visible light [47].

3.1.4. XRD pattern

The XRD patterns of SBA-15, $\text{TiO}_2(18.2\%)/\text{SBA-15}$, and $\text{RuO}_{2(6.4\%)}\text{-TiO}_2(16.9\%)/\text{SBA-15}$ are presented in Fig. 6. The successful formation of SBA-15 is confirmed by the presence of a broad region between 20° and 30° in 2θ, which is characteristic of amorphous silica [20,48,49]. According to Thahir et al. [48], this amorphous peak approach at 2θ = 23° can be attributed to the (100) planar orientation with hexagonal symmetry (p6mm). In the presence of TiO_2 , new diffraction peaks appear at 2θ = 25.4°, 37.8°, 48.1°, 54.5° and 62.8° equivalent to (101), (110), (200), (210) and (300) lattice planes of the anatase phase of TiO_2 , respectively [20]. Anatase was the only TiO_2 phase formed, as the rutile diffraction peaks were not observed. For the material loaded with Ru-oxide, the characteristic diffraction peaks of the RuO_2 were reported in 2θ = 28.0° and 35.2°, equivalent to (110) and (101) lattice planes of the RuO_2 , respectively [50].

3.1.5. High-resolution XPS spectra

XPS analysis further confirms the purity of the fresh $\text{RuO}_{2(6.4\%)}\text{-TiO}_2(16.9\%)/\text{SBA-15}$ composite, showing the elemental composition of O, Ti, Si, and Ru in the survey spectra (Fig. 7a). The Si 2p occupied state spectrum (Fig. 7b.1) reveals binding energies of 103.9, 101.9, and 100.2 eV, which can be ascribed to Si-O, Si-O_x, and Si-O-Ti compounds, respectively. In addition, the C1s + Ru 3d combined spectrum (Fig. 7b.2) is composed of the C1s reference signal (284.6 eV), along with the Ru signals predominantly at 280.4 eV for Ru 3d_{5/2} orbital, indicating the presence of Ru-O in the 2+ oxidation state [51,52]. The Ru 3p + Ti 2p composed spectrum (Fig. 7b.3) is represented by the orbitals 2p_{3/2} (458.0 eV) and 2p_{1/2} (463.4 eV) that are referenced to titanium dioxide. Additionally, in this same electron shell, the presence of Ru from 468 to 490 eV, assigned to the Ru 3p_{1/2} and Ru 3p_{3/2} regions, can be associated with the change ligand screening at charge-transfer configurations caused by the junction of the Ru and Ti elements [53]. The O 1 s spectrum in Fig. 7b.4 illustrates the pristine mesoporous silica functionalised with TiO_2 , showcasing the Si-O-Ti peak at 531.7 eV [54]. Additionally, the surface of the catalytic material displays peaks corresponding to lattice oxygen at 528.4 eV [55] and 533.8 eV [56]. The discussion concerning XPS analysis performed on the photocatalytic sample after the 10th cycle of utilization (Fig. 7c) will be explored in Section 3.2.6.

3.2. Photocatalytic activity

The kinetics of CO_2 reduction for all thermo-photocatalytic reactions followed a pseudo-first-order kinetic model (coefficient of determination (R^2) > 0.90). All the corresponding kinetic parameters and reaction efficiency indicators are reported in Table 2. It should also be mentioned that the main product of CO_2 hydrogenation was CH_4 , with C_2H_6 being less than 0.2 %. CO or higher hydrocarbons were below the equipment detection limit.

3.2.1. Effect of the photocatalyst composition

Fig. 8a and Fig. 8b show the photocatalytic activity of the hybrid material (150 °C, $[\text{CO}_2]:[\text{H}_2]$ molar ratio of 1:4, RP of 0.45 W) containing different doses of (i) TiO_2 over the SBA-15 silica support, in the absence and the presence of RuO_2 (keeping an $[\text{Ru}]:[\text{TiO}_2/\text{SBA-15}]$ mass ratio of 0.8:10), and (ii) RuO_2 over the $\text{TiO}_2/\text{SBA-15}$ nanocomposite (keeping a $[\text{TiO}_2]:[\text{SBA-15}]$ mass ratio of 2:10), respectively. In absence of the RuO_2 , the conversion of CO_2 into CH_4 was negligible (< 6.5 %) regardless of the amount of TiO_2 on the SBA-15 support (Table 2, experiments #1.1 to #1.3). Such a low performance can potentially be explained by two factors [57,58]: (i) as TiO_2 is an n-type oxide semiconductor, prone to oxygen vacancy defects, it acts as an electron donor to the lattice elements, and (ii) TiO_2 redox potential for conduction band electrons (-0.52 V) is not enough to compensate for the single-electron reduction potential of CO_2 to the carboxyl radical $\text{CO}_2^\bullet-$ ($E^0 = -1.9$ V vs. NHE). Besides, n-type semiconductors are usually applied to promote photocatalytic oxidation reactions, instead of the photoreduction ones, since interfacial electrons flow out from the semiconductor to attain equilibrium, lowering the Fermi level (located slightly below the conduction band) energy and generating a potential gradient that moves the valence band holes toward the semiconductor interface. Conversely, p-type semiconductors are commonly employed in photocatalytic reduction reactions since the electrons on the conduction band migrate up to the semiconductor interface due to a band bending gradient caused by the Fermi level (located slightly above the valence band) energy increase [57,58].

On the other hand, with the incorporation of RuO_2 in the SBA-15, CO_2 reduction efficiency increased up to 22.7 % (Table 2, experiment #1.4). Depending on some factors, such as atmosphere redox nature, molecular structure and/or thin film morphology, RuO_2 can feature a p-type electrical conductivity behaviour, despite being an n-type conductor at room temperature when stoichiometric, or closer so, contrary to pure Ru, which is a p-type compensated metal [59,60]. For instance, it was found a change in the dominant charge carrier from electrons to holes, i.e., from n-type to p-type carriers, on the RuO_2 metal when [60]: (i) the average film grain size was reduced, owing to a fast-deposition-rate procedure at low substrate temperature; (ii) the oxygen was progressively lost from RuO_2 films to a two-phase mixture of RuO_2 and Ru, as a result of film strains, non-stoichiometric surfaces, and point and/or extended defects; and (iii) the atmosphere was switched from oxidising (O_2) to a reducing (CO) one at 250 °C due to the loss of interior oxygen, after the depletion of the oxygen at the free and grain boundary surfaces. However, even using a material potentially oriented to photoreduction reactions, CO_2 conversion was still low since it is difficult for a single-component photocatalyst to possess both a wide light absorption range and a sizable redox ability to attain high CO_2 reduction efficiencies.

To enhance the electrical proprieties of the photocatalytic material, both TiO_2 and RuO_2 photocatalysts can be combined over the SBA-15 support. According to Jin et al. [61], Ru/black TiO_2 catalysts have good responsiveness to synergistic utilization of light and heat during the conversion of CO_2 . Furthermore, modifying an n-type semiconductor by loading it with suitable p-type metal oxide nanoparticles can form a composite structure working as a Z-scheme system, which is more effective in promoting CO_2 photocatalytic reduction [58,62]. The distinct catalytic structure composed of SBA-15 decorated with RuO_2 :

Table 2

Main operating conditions and methanation reaction performance indicators for each experiment.

Trial #	Photocatalyst		Rectional system				CO ₂ reduction				CH ₄ generation			Φ^{APE} (%)	Φ^{AQY} (%)
	Composition	Mass (mg)	Uses	T (°C)	[CO ₂]:[H ₂] (mol:mol)	RP (W)	$k \times 10^2$ (min ⁻¹)	R ²	r_0 (mM min ⁻¹)	X _{CO₂} (%)	Y _{CH₄} (%)	S _{CH₄} (%)	P _{CH₄} (mmol g _{cat} ⁻¹ h ⁻¹)	P _{CH₄} (mmol g _{active_cat} ⁻¹ h ⁻¹)	
Effect of the photocatalyst composition (Section 3.2.1, Fig. 8)															
<i>Variation of the TiO₂ loading on SBA-15 in the absence of RuO₂</i>															
1.1	TiO ₂ (10.0%)/SBA-15	30	1 st	150	1:4	0.45 ± 0.01	-	-	-	-	-	-	-	-	
1.2	TiO ₂ (18.2%)/SBA-15						0.064 ± 0.005	0.974	0.008 ± 0.001	6.4	6.4	100	0.6	3.3	
1.3	TiO ₂ (28.2%)/SBA-15						0.013 ± 0.006	0.907	0.0017 ± 0.0009	1.8	1.8	100	0.2	0.6	
<i>Variation of the TiO₂ loading on SBA-15 in the presence of RuO₂ [Ru:TiO₂/SBA-15 = 0.8:10 (w/w)]</i>															
1.4	RuO ₂ (8.8%)/TiO ₂ (9.3%)/SBA-15	30	1 st	150	1:4	0.45 ± 0.01	0.24 ± 0.02	0.983	0.033 ± 0.002	22.7	22.7	100	2.2	25.2	
1.5	RuO ₂ (4.7%)/TiO ₂ (9.3%)/SBA-15						1.4 ± 0.1	0.976	0.19 ± 0.02	85.1	85.0	99.9	7.9	56.2	
1.6	RuO ₂ (6.4%)/TiO ₂ (16.9%)/SBA-15						2.1 ± 0.3	0.960	0.28 ± 0.05	98.5	98.3	99.8	9.2	39.7	
1.7	RuO ₂ (5.5%)/TiO ₂ (26.1%)/SBA-15						1.1 ± 0.1	0.959	0.14 ± 0.02	72.3	72.2	99.8	6.7	21.2	
<i>Variation of the RuO₂ loading on TiO₂/SBA-15 [TiO₂:SBA-15 = 2:10 (w/w)]</i>															
1.8	RuO ₂ (3.0%)/TiO ₂ (17.5%)/SBA-15	30	1 st	150	1:4	0.45 ± 0.01	1.2 ± 0.1	0.976	0.17 ± 0.02	75.1	75.1	100	7.0	34.2	
1.6	RuO ₂ (6.4%)/TiO ₂ (16.9%)/SBA-15						2.1 ± 0.3	0.960	0.28 ± 0.05	98.5	98.3	99.8	9.4	40.3	
1.9	RuO ₂ (11.7%)/TiO ₂ (16.3%)/SBA-15						2.3 ± 0.3	0.975	0.31 ± 0.04	98.5	98.4	99.9	9.5	33.8	
1.10	RuO ₂ (13.9%)/TiO ₂ (15.7%)/SBA-15						2.0 ± 0.3	0.966	0.26 ± 0.04	96.9	96.9	100	8.9	30.1	
1.11	RuO ₂ (16.7%)/TiO ₂ (15.2%)/SBA-15						1.9 ± 0.3	0.968	0.26 ± 0.04	92.9	92.9	99.9	8.9	27.8	
Effect of the photocatalyst loading (Section 3.2.2, Fig. 9)															
1.6	RuO ₂ (6.4%)/TiO ₂ (16.9%)/SBA-15	30	1 st	150	1:4	0.45 ± 0.01	2.1 ± 0.3	0.960	0.28 ± 0.05	98.5	98.3	99.8	9.4	40.4	
2.1		20					2.7 ± 0.4	0.975	0.36 ± 0.05	99.4	99.2	99.8	13.9	59.7	
2.2		10					1.18 ± 0.08	0.988	0.16 ± 0.01	72.7	72.5	99.7	19.9	85.5	
Effect of the illumination source and power (Section 3.2.3, Fig. 10)															
<i>Polychromatic irradiation - simulated sunlight illumination</i>															
3.1	RuO ₂ (6.4%)/TiO ₂ (16.9%)/SBA-15	20	1 st	150	1:4	0.211 ± 0.004	2.1 ± 0.3	0.969	0.28 ± 0.04	96.8	96.6	99.8	13.6	58.6	
3.2						0.339 ± 0.006	2.3 ± 0.3	0.977	0.32 ± 0.04	98.3	98.2	99.9	14.3	61.3	
2.1						0.45 ± 0.01	2.7 ± 0.4	0.975	0.36 ± 0.05	99.4	99.2	99.8	13.9	59.7	
3.3						1.09 ± 0.03	2.4 ± 0.3	0.970	0.32 ± 0.05	99.2	99.2	100	14.1	60.6	
<i>Monochromatic irradiation - microscale illumination using LED at 365nm</i>															
3.4	RuO ₂ (6.4%)/TiO ₂ (16.9%)/SBA-15	20	1 st	150	1:4	0.053 ± 0.009	0.73 ± 0.03	0.968	0.097 ± 0.005	58.4	58.3	99.8	8.1	34.9	
3.5						0.17 ± 0.03	0.98 ± 0.03	0.951	0.131 ± 0.008	68.7	68.7	99.9	9.4	40.4	
3.6						0.30 ± 0.05	1.51 ± 0.06	0.966	0.20 ± 0.01	87.3	87.1	99.8	12.2	52.3	
3.7						0.55 ± 0.08	2.0 ± 0.5	0.970	0.27 ± 0.07	98.5	98.3	99.8	14.3	61.3	
<i>Monochromatic irradiation - microscale illumination using LED at 405 nm</i>															
3.8	RuO ₂ (6.4%)/TiO ₂ (16.9%)/SBA-15	20	1 st	150	1:4	0.055 ± 0.008	0.9 ± 0.4	0.970	0.13 ± 0.05	65.6	65.4	99.7	9.1	39.3	
3.9						0.18 ± 0.02	1.27 ± 0.03	0.981	0.168 ± 0.007	78.6	78.6	100	11.1	47.4	
3.10						0.37 ± 0.06	1.56 ± 0.07	0.972	0.21 ± 0.01	88.2	88.0	99.9	12.4	53.2	
3.11						0.55 ± 0.07	1.6 ± 0.4	0.982	0.22 ± 0.06	88.8	88.7	99.9	12.5	53.5	
Effect of the H₂:CO₂ molar ratio (Section 3.2.4, Fig.11)															
4.1	RuO ₂ (6.4%)/TiO ₂ (16.9%)/SBA-15	20	1 st	150	1:2	0.211 ± 0.004	0.7 ± 0.3	0.923	0.10 ± 0.04	51.8	51.7	99.8	7.2	31.1	
3.1					1:4	2.1 ± 0.3	0.969	0.28 ± 0.04	96.8	96.6	99.8	13.6	58.6		
4.2					1:7	2.4 ± 0.3	0.980	0.32 ± 0.04	95.6	95.4	99.8	13.8	59.3		

(continued on next page)

Table 2 (continued)

Trial #	Photocatalyst	Reactional system						CO ₂ reduction			CH ₄ generation			Φ^{APE} (%)	Φ^{AQY} (%)												
		Composition	Mass (mg)	Uses	T (°C)	[CO ₂]:[H ₂] (mol:mol)	RP (W)	$k \times 10^2$	R^2	r_0 (mM min ⁻¹)	X_{CO_2} (%)	Y_{CH_4} (%)	S_{CH_4} (%)	P_{CH_4} (mmol g _{cat} ⁻¹ h ⁻¹)													
								(min ⁻¹)						P_{CH_4} (mmol g _{active_cat} ⁻¹ h ⁻¹)													
Effect of the reaction temperature (Section 3.2.5, Fig.12)																											
<i>Under dark conditions – Thermal catalysis</i>																											
5.1	RuO _{2(6.4%)} :TiO _{2(16.9%)} /SBA-15	20	1 st	50	1:4	-		0.002 ± 0.001	0.941	0.0003 ± 0.0001	0.3	0.3	100	0.0	0.2	-	-										
5.2				100				0.34 ± 0.03	0.972	0.046 ± 0.004	31.8	31.8	100	4.5	19.5	-	-										
5.3				150				0.96 ± 0.06	0.988	0.128 ± 0.009	65.6	65.4	99.7	9.2	39.4	-	-										
5.4				200				2.3 ± 0.4	0.956	0.30 ± 0.05	96.6	96.4	99.8	13.4	57.6	-	-										
5.5				250				3.6 ± 0.5	0.978	0.47 ± 0.07	99.7	99.7	100	13.5	57.9	-	-										
<i>Under light conditions – Thermo-photocatalysis</i>																											
5.6	RuO _{2(6.4%)} :TiO _{2(16.9%)} /SBA-15	20	1 st	50 ^a	1:4		0.211 ± 0.004	0.008 ± 0.001	0.930	0.0010 ± 0.0001	0.8	0.8	100	0.1	0.5	0.1	0.1										
5.7				100				0.55 ± 0.04	0.985	0.075 ± 0.005	46.3	46.2	99.6	6.5	27.9	10.4	11.1										
3.1				150				2.1 ± 0.3	0.969	0.28 ± 0.04	96.8	96.6	99.8	13.6	58.4	39.4	42.0										
5.8				200				3.1 ± 0.6	0.957	0.41 ± 0.08	98.1	98.1	100	13.8	59.4	57.0	60.7										
5.9				250				3.7 ± 0.3	0.991	0.49 ± 0.05	99.1	99.1	100	14.1	60.7	68.4	72.8										
Effect photocatalyst reuse (Section 3.2.6, Fig. 13)																											
<i>Reuse of the photocatalyst without reactivation between cycles</i>																											
3.1	RuO _{2(6.4%)} :TiO _{2(16.9%)} /SBA-15	20	1 st	150	1:4		0.211 ± 0.004	2.1 ± 0.3	0.969	0.28 ± 0.04	96.8	96.6	99.8	13.6	58.5	39.5	42.1										
6.1			2 nd					1.8 ± 0.2	0.969	0.24 ± 0.03	93.4	93.3	99.9	12.9	55.3	32.9	35.0										
6.2			3 rd					1.4 ± 0.2	0.948	0.18 ± 0.03	83.7	83.5	99.8	12.0	51.5	25.6	27.3										
6.3			4 th					1.2 ± 0.2	0.957	0.15 ± 0.02	81.3	81.2	99.9	11.1	47.5	21.4	22.7										
6.4			5 th					1.0 ± 0.1	0.951	0.13 ± 0.02	76.5	76.4	99.9	10.4	44.7	18.6	19.8										
6.5			6 th					1.0 ± 0.2	0.924	0.14 ± 0.03	79.7	79.6	99.9	11.4	49.0	19.6	20.9										
6.6			7 th					0.9 ± 0.1	0.969	0.12 ± 0.01	67.4	67.3	99.9	9.5	40.7	17.3	18.4										
6.7			8 th					0.9 ± 0.1	0.970	0.13 ± 0.01	68.6	68.6	99.9	9.8	42.0	17.7	18.8										
6.8			9 th					0.86 ± 0.07	0.981	0.12 ± 0.01	62.1	62.0	99.9	9.0	38.5	16.3	17.4										
6.9			10 th					0.82 ± 0.07	0.976	0.11 ± 0.01	61.0	60.9	99.9	8.7	37.5	15.5	16.5										
<i>Effect of the water presence</i>																											
6.10	RuO _{2(6.4%)} :TiO _{2(16.9%)} /SBA-15	20	1 st	150	1:4+H ₂ O ^b		0.211 ± 0.004	0.42 ± 0.07	0.911	0.06 ± 0.01	39.7	39.6	99.7	5.5	23.7	7.8	8.3										
<i>Reuse of the photocatalyst with reactivation between cycles^c</i>																											
6.11	RuO _{2(6.4%)} :TiO _{2(16.9%)} /SBA-15	20	1 st	150	1:4		0.211 ± 0.004	2.1 ± 0.3	0.969	0.28 ± 0.04	96.8	96.6	99.8	13.4	57.3	38.5	41.0										
6.12			2 nd					2.0 ± 0.3	0.973	0.27 ± 0.04	93.6	93.4	99.8	13.2	56.8	38.0	40.5										
6.13			3 rd					1.9 ± 0.2	0.956	0.25 ± 0.03	92.7	92.6	99.9	13.0	56.0	28.2	37.9										

^a Experiment equated to a methanation reaction via photocatalysis (without external heating) since the temperature of 50 °C is the lowest feasible, as it coincides with the minimum temperature value that can be achieved inside the Suntest's chamber.

^b Addition of 14.5 µL of ultrapure water.

^c Reutilization of the photocatalyst applying nitrogen flux at high temperature between the experiments to remove the steam water generated from the methanation reaction.

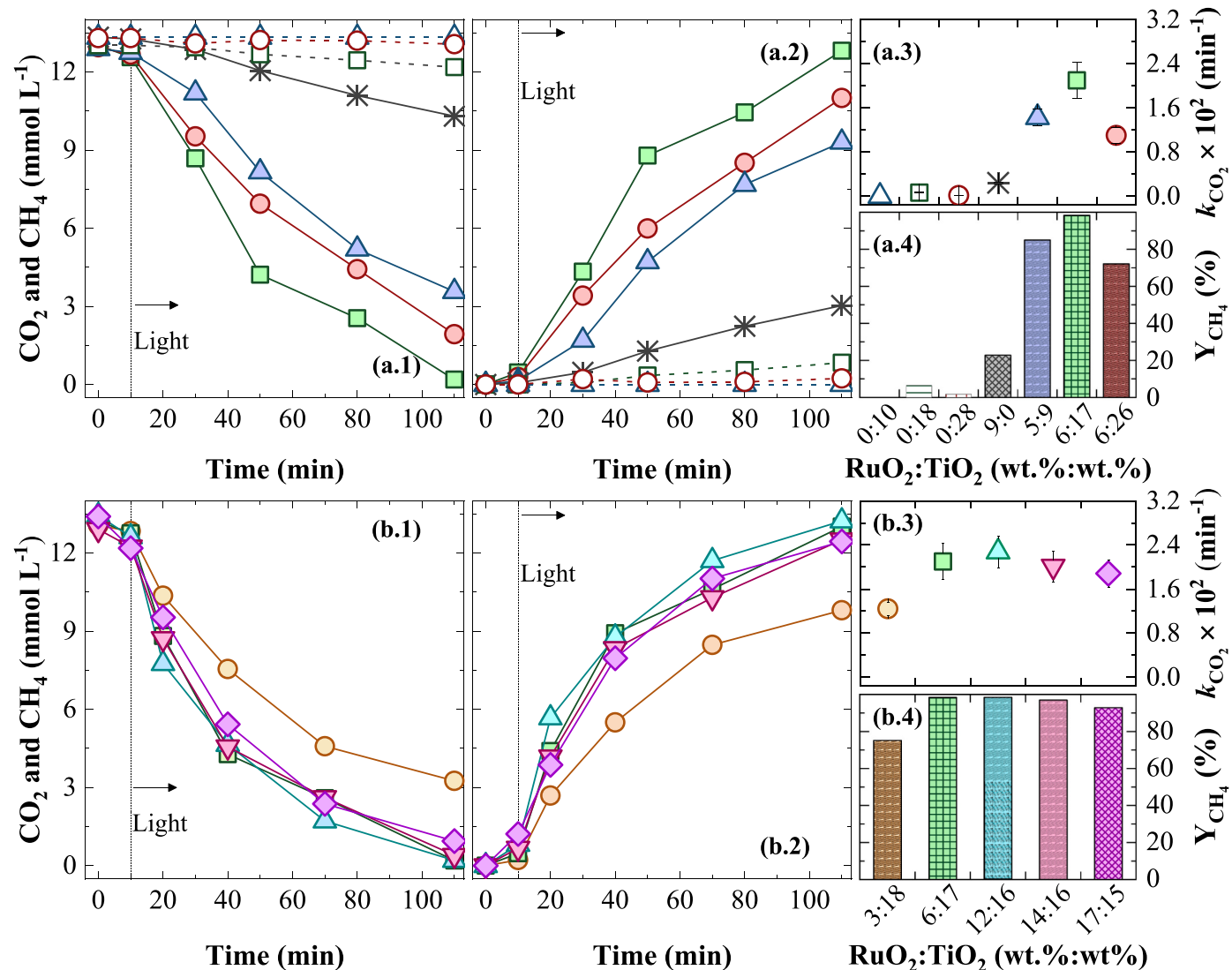


Fig. 8. Temporal profile of the solar-driven thermo-photocatalytic conversion of (.1) CO₂ into (.2) CH₄, along with the (.3) pseudo-first-order kinetic constants for CO₂ reduction and (.4) CH₄ production yields, using different RuO_{2(x%)}:TiO_{2(y%)}/SBA-15 catalyst compositions (where x and y are the amounts of RuO₂ and TiO₂, respectively, expressed in wt%): (a) variation of the (y%) TiO₂ load on the SBA-15 support in the absence (open symbols) and the presence (solid symbols) of (x%) RuO₂, maintaining the [Ru]:[TiO₂/SBA-15] mass ratio at 0.8:10 (with x%:y% equal to 0:10 (- - △ -), 0:18 (- - □ -), 0:28 (- - ○ -), 9:0 (- * -), 5:9 (- ▲ -), 6:17 (- ■ -), and 6:26 (- ● -)); and (b) variation of the (x%) RuO₂ load on the TiO_{2(y%)}/SBA-15 nanocomposite, keeping the [TiO₂]:[SBA-15] mass ratio at 2:10 (with x%:y% equal to 3:18 (- ○ -), 6:17 (- □ -), 12:16 (- ▲ -), 14:16 (- ▽ -), and 17:15 (- ▾ -)). Operating conditions: V = 40 mL; P_{CO₂} = 0.32 bar; P_{H₂} = 1.28; 30 mg of photocatalyst; T = 150 °C; and RP = 0.45 W.

TiO₂ proved to be a viable alternative for the thermo-photoreduction of CO₂, reaching conversions between 72.3 % and 98.5 %, with almost 100 % selectivity for CH₄ (Table 2, experiments #1.5 to #1.7).

From Fig. 8a, it was possible to verify that increasing the TiO₂ load from 9.3 % to 16.9 % (corresponding to [TiO₂]:[SBA-15] mass ratios of 1:10 and 2:10, respectively) in the RuO_{2(4.7-6.4%)}:TiO₂/SBA-15 nanocomposite (Table 2, experiments #1.5 and 1.6), while maintaining the [Ru]:[TiO₂/SBA-15] mass ratio at 0.8:10, led to a significant improvement on the CO₂ thermo-photoconversion (Fig. 8a.1), doubling the CH₄ yield right after 30-min reaction (Fig. 8a.2) and the pseudo-first-order kinetic constant for CO₂ reduction (Fig. 8a.4). As expected, the methanation reaction performance was boosted as the number of active centres on the structured material expanded. Moreover, the good molecular dispersion of Ti and Ru oxides in SBA-15 mesoporous silica prevented

particle agglomeration. It thereby reduced the internal electron-holes recombination and the shading effect, which hinders the light absorption by the semiconductor [37,42]. However, the over-loading of TiO₂ nanoparticles, achieved for a mass percentage of 26.1 % (Table 2, experiment #1.7), may have started the formation of clusters, which resulted in the physical blockage of the SBA-15 mesopores, thus compromising CO₂ conversion (roughly 25 %) due to mass and photon transfer limitations [14,42,63]. Therefore, a [TiO₂]:[SBA-15] mass ratio of 2:10, the equivalent of 16.9 % TiO₂, was chosen for the trials regarding the RuO₂ content optimization. Similar results were noticed by Chen et al. [14], where higher CO₂ photoreduction efficiencies were obtained using ca. 20 % TiO₂ in SBA-15 loaded with CdS.

CO₂ reduction and CH₄ production kinetics showed similar profiles for RuO₂ concentrations higher than 6.4 %, the equivalent to a [Ru]:

[$\text{TiO}_2/\text{SBA-15}$] mass ratio of 0.8:10, as displayed in Fig. 8b. Two opposite effects can be observed: (i) enriching the photocatalytic material with RuO_2 increases the number of photoactive sites, boosting the methanation efficiency [11,64]; (ii) loading the photocatalytic material with RuO_2 in excess can shorten the distance between the nanoparticles and act as an electron-hole recombination centre. Additionally, RuO_2 in excess occupies the catalytically active sites, thus reducing the specific catalytic surface area, which declines the CH_4 production yield [65]. In this sense, the occurrence of both effects was experimentally checked when the RuO_2 percentage was raised: (i) from 3.0 % to 6.4/11.7 % (Table 2, experiments #1.8 to #1.6/#1.9, respectively), improving the CO_2 conversion efficiency after 110 min from 75.1 % to 98.5 % (Fig. 8b.1–2, 4) and the kinetic constants for CO_2 reduction from $(1.2 \pm 0.1) \times 10^{-2}$ to $(2.1 \pm 0.03) \times 10^{-2}/(2.3 \pm 0.3) \times 10^{-2} \text{ min}^{-1}$ (Fig. 8b.3); and (ii) from 6.4/11.7–16.7 % (Table 2, experiments #1.6/#1.9 to #1.11, respectively), resulting in a slight drop in the CO_2 conversion up to 92.9 % (Fig. 8b.1–2, 4) and the kinetic constant decreased to $(1.9 \pm 0.3) \times 10^{-2} \text{ min}^{-1}$ (Fig. 8b.3).

Given all the obtained results, the $\text{RuO}_{2(6.4\%)}:\text{TiO}_{2(16.9\%})/\text{SBA-15}$ nanocomposite (Table 2, experiment #1.6) was selected as the optimal photocatalytic material to be used in the subsequent methanation experiments, considering the best compromise between the highest CO_2 conversion at the lowest RuO_2 content. Due to the high selectivity as regards CH_4 product, the CO_2 concentration history will not be displayed for the remaining trials to avoid redundancies.

3.2.2. Effect of the photocatalyst dose

Fig. 9 illustrates the influence of $\text{RuO}_{2(6.4\%)}:\text{TiO}_{2(16.9\%})/\text{SBA-15}$ photocatalyst mass on the specific (Fig. 9a) and the overall (Fig. 9a; inset) CH_4 production (150°C , $[\text{CO}_2]:[\text{H}_2]$ molar ratio of 1:4, $RP = 0.45 \text{ W}$) expressed in $\text{mmol g}_{\text{cat}}^{-1}$ and mmol L^{-1} , respectively. Although lowering the photocatalyst dose from 30 to 20 mg (Table 2, experiments #1.6 and #2.1) implied a similar overall CH_4 concentration of around 13 mmol L^{-1} after 110 min, the specific production was increased by 48 %, from 17.2 to 25.5 mmol CH_4 per gram of catalyst. This behaviour suggests that, within the limits of the experimental system set-up, the overall CO_2 thermo-photoconversion is virtually unaffected (98.3–99.2 %) by using catalyst masses higher than 20 mg since this amount is enough to absorb the photons reaching inside the reactor. In fact, using

30 mg of photocatalyst led to a slight decrease (20 %–22 %) in the values of the photonic efficiencies (Fig. 9c) and kinetic constants for CO_2 reduction (Fig. 9b), indicating photon-transfer limitations potentially by particles overloading. Conversely, the inverse effect occurred by lowering the catalyst mass from 20 to 10 mg (Table 2, experiments #2.1 and #2.2), with the overall CH_4 production (Fig. 9a; inset) and the CO_2 kinetic constants (Fig. 9b) being reduced by 56 % and 27 %, respectively. Moreover, the specific CH_4 production (Fig. 9a) was increased to around 36 $\text{mmol g}_{\text{cat}}^{-1}$ after 110 min, while photonic efficiency was compromised by 56 % (Fig. 9c). In this case, the decrease in the photocatalyst amount implied a lower electron-hole pairs generation by the lack of photoactive sites, thus impairing reaction efficiency. Therefore, 20 mg of $\text{RuO}_{2(6.4\%)}:\text{TiO}_{2(16.9\%})/\text{SBA-15}$ was selected for the following methanation tests as it led to a higher molar conversion efficiency.

The main disadvantage of using semiconductors loaded with metal or non-metal nanoparticles is the occurrence of electron-hole pairs recombination centres [66]. Nonetheless, employing a mesostructured silica material, such as SBA-15, as a support of this kind of photocatalyst can result in spatial charge separation and, consequently, a photocatalytic conversion differential [37,42,63], as represented in this work with a CO_2 photoconversion of 99.4 % after 110 min (Table 2, experiment #2.1). To the best of our knowledge, available bibliographic data so far regarding catalytic activities (see Table S4) have indicated that this novel $\text{RuO}_{2(6.4\%)}:\text{TiO}_{2(16.9\%})/\text{SBA-15}$ photocatalyst is among the most efficient metal-based materials for photo-assisted CO_2 methanation at low temperatures, achieving an average specific CH_4 production rate of $13.9 \text{ mmol g}_{\text{cat}}^{-1} \text{ h}^{-1}$ at 150°C (Table 2, experiment #2.1). It should also be noted that using SBA-15 in the nanostructured material composition requires fewer photoactive catalyst phases, i.e., TiO_2 and RuO_2 . Such an aspect is highly relevant because ruthenium is an expensive noble metal, and minimising its content is essential for a cost-effective process. So, if we consider that only 23.3 % of the catalytic material composed of TiO_2 and RuO_2 (Table S1) is actually photoactive, the specific CH_4 production rate increases about 4-fold, resulting in $59.7 \text{ mmol}_{\text{CH}_4} \text{ g}_{\text{active cat}}^{-1} \text{ h}^{-1}$ or $286.1 \text{ mmol}_{\text{CH}_4} \text{ g}_{\text{Ru}}^{-1} \text{ h}^{-1}$, using simulated solar irradiation with an RP of 0.45 W. Comparing this productivity value, which accounts only for the active photocatalyst, with the literature reports on unsupported Ru-based catalysts (Table S4) under similar irradiation (Xe Lamp/Vis-NIR light) and temperatures (140/150

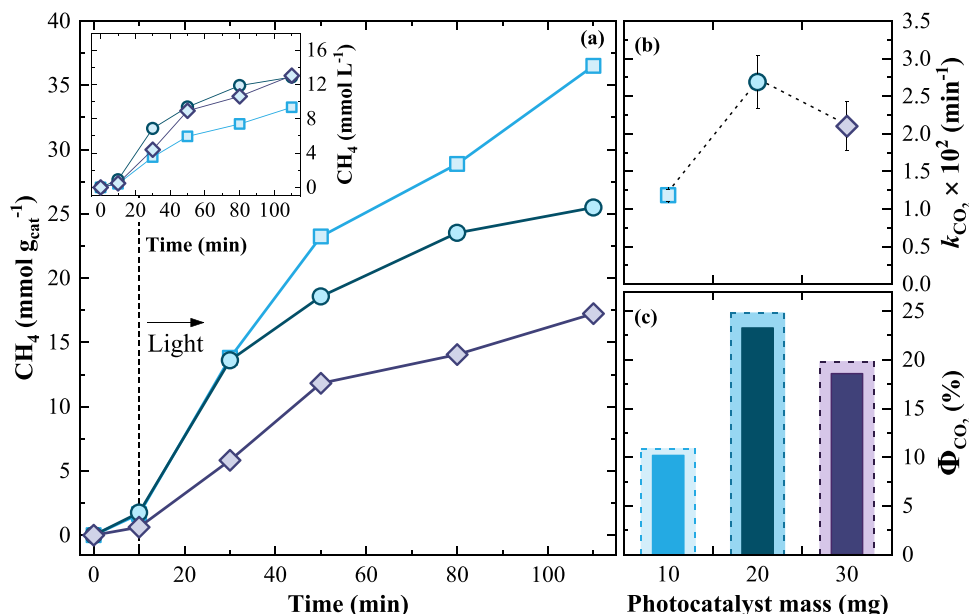


Fig. 9. Representation of the (a) solar-driven thermo-photocatalytic production of CH_4 over time, expressed in mmol per gram of photocatalyst and mmol per litre (inset), along with the (b) pseudo-first-order kinetic constants for CO_2 reduction and (c) apparent photonic efficiency (solid line bars) and apparent quantum yield (dash line bars), using different amounts of the $\text{RuO}_{2(6.4\%)}:\text{TiO}_{2(16.9\%})/\text{SBA-15}$ photocatalyst: 10 mg (open squares); 20 mg (filled circles); and 30 mg (open diamonds). Operating conditions: $V = 40 \text{ mL}$; $P_{\text{CO}_2} = 0.32 \text{ bar}$; $P_{\text{H}_2} = 1.28$; $T = 150^\circ\text{C}$; and $RP = 0.45 \text{ W}$.

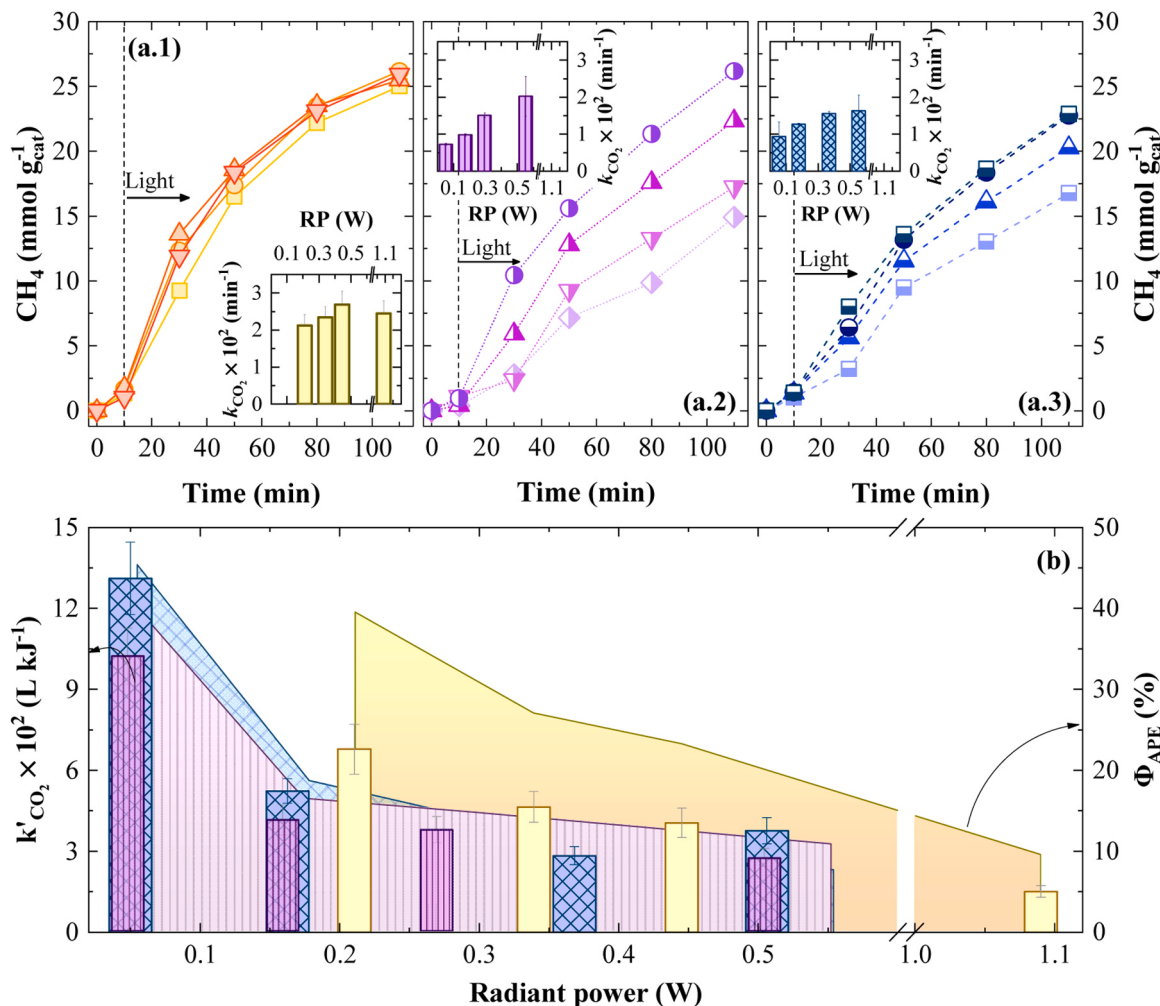


Fig. 10. Representation of the (a) thermo-photocatalytic production of CH_4 over time, along with the time-based pseudo-first-order kinetic constants for CO_2 reduction (inset), and (b) apparent photonic efficiency (area), together with the energy-based pseudo-first-order kinetic constants for CO_2 reduction (bars), using different illumination sources and radiant power: (a.1) polychromatic simulated sunlight (yellow bars), with RPs of 0.211 (yellow square), 0.339 (orange circle), 0.45 (red triangle), and 1.09 (red inverted triangle) W; (a.2) monochromatic UV-LED at 365 nm (purple bars), with RPs of 0.053 (purple diamond), 0.17 (purple inverted triangle), 0.30 (purple triangle), and 0.55 (purple circle) W; and (a.3) monochromatic Vis-LED at 405 nm (blue bars), with RPs of 0.055 (blue square), 0.18 (blue triangle), 0.37 (blue circle), and 0.55 (blue square) W. Operating conditions: $V = 40 \text{ mL}$; $P_{\text{CO}_2} = 0.32 \text{ bar}$; $P_{\text{H}_2} = 1.28$; 20 mg of $\text{RuO}_{2(6.4\%)}:\text{TiO}_{2(16.9\%)}/\text{SBA-15}$ photocatalyst; and $T = 150^\circ\text{C}$.

, an 2.9- and 4.1-fold improvement can be observed. Such a performance, even at low temperatures, can be attributed to the increased surface area provided by the SBA-15 support (Table S3), which enhanced light harvesting and mass transfer efficiency [29].

3.2.3. Effect of the illumination source and power

Upon irradiation, an electron-changeover from the valence to the conduction band of the photocatalyst occurs, being the electrons further used in the CO_2 reduction reaction. Notwithstanding, the effect of distinct illumination sources on CO_2 photoconversion is poorly understood. Despite Sun being the most sustainable irradiation source and, as such, the most pursued worldwide to assist photocatalytic processes, the polychromatic solar light is limited to the time of the day, the season of the year, and the geographic location. Therefore, its use must indeed be prioritised, but complementary lighting sources must be studied. In this sense, the miniaturised monochromatic illumination sources can be an attractive alternative for a more “customised” irradiation profile, resulting in a more efficient catalytic surface illumination [67]. Accordingly, the thermo-photocatalytic CO_2 methanation (20 mg of $\text{RuO}_{2(6.4\%)}:\text{TiO}_{2(16.9\%)}/\text{SBA-15}$, 150 °C, $[\text{CO}_2]:[\text{H}_2]$ molar ratio of 1:4)

was evaluated under two different illumination sources (Fig. 10): (i) polychromatic, through a sunlight simulator, emitting radiation between 280 and 800 nm (Table 2, experiments #2.1 and #3.1 to #3.3); and (ii) monochromatic, through a UV LED at 365 nm (Table 2, experiments #3.4 to #3.7) and a Visible LED at 405 nm (Table 2, experiments #3.8 to #3.11). The effect of different radiant power (RP) values reaching inside the photoreactor was also assessed for all lighting devices. Overall, the photocatalytic activity of the $\text{RuO}_{2(6.4\%)}:\text{TiO}_{2(16.9\%)}/\text{SBA-15}$ nanocomposite towards CO_2 reduction rate is ranked in the descending order, in terms of the illumination source, as follows: sunlight (initial CO_2 reaction rate of 0.28–0.36 mM min⁻¹, for RP from 0.211 to 1.09 W) > 405 nm LED (0.13–0.22 mM min⁻¹, for RP from 0.055 to 0.55 W) > 365 nm LED (0.097–0.27 mM min⁻¹, for RP from 0.053 to 0.55 W).

Regarding simulated solar irradiation, there was only a slight decrease in the time-based kinetic constant for CO_2 reduction (Fig. 10a: inset), with the decline of the RP from 1.09/0.45–0.21 W (maximum and minimum irradiation limits allowed by the Suntest®). Also, there was virtually no difference in the CH_4 production yield, being converted more than 96 % of CO_2 after 110 min (Table 2, experiments #2.1 and

#3.1 to #3.3), regardless of the photon flux reaching the photocatalyst surface. Conversely, the lower the RP, the higher the energy-based kinetic constant for CO₂ reduction and the higher the apparent photonic efficiency (Fig. 10b), suggesting that as the power increased, photons in excess were being generated and were not being used to excite the photocatalyst's electrons. Moreover, since the reaction rate was practically unchanged when the solar radiation intensity decreased (Fig. 10a.1), the apparent quantum yield increased from 10.2 % to 42.1 %, which is higher than those commonly found in the literature (ranging between 0.25 % and 12.4 %) [68,69]. Therefore, the optimal thermo-photocatalytic performance of the RuO_{2(6.4%):TiO_{2(16.9%)}}/SBA-15 material was obtained for an RP of 0.21 W (the equivalent to an irradiance of 167 W m⁻², considering that the reactor window diameter is 40 mm), the lowest value allowed by the sunlight simulator, achieving the highest photonic efficiency of 39.5 % (Fig. 10b, Table 2, experiment #3.1). This high value may have resulted from thermal enhancement over the plasmonic structures due to the synergistic effect between the combined plasmon-induced hot carrier generation, hot electron transfer, and thermalization processes resulting from the metal/semiconductor heterojunction. Besides that, non-plasmonic structures can also demonstrate a photo-thermal effect via direct interband and intraband electronic transitions analogously to the plasmonic components [70]. Moreover, incorporating the active photocatalyst into the SBA-15 support increases the surface area, improving light harvesting, surface sites, and mass transfer [29]. Thus, such an outcome may be explained by the combination of the thermo-photocatalytic process and the exceptional absorption capability of the photocatalytic material across all the UV-Vis-IR regions (see Fig. 5). In these conditions (Table 2, experiment #3.1), a 96.8 % CO₂ conversion and average specific CH₄ production rates of 13.6 mmol g_{cat}⁻¹ h⁻¹ and 58.6 mmol g_{active,cat}⁻¹ h⁻¹ (280.7 mmolCH₄ g_{Ru}⁻¹ h⁻¹) were reached, which is among some of the highest values found in the literature (Table S4). For instance, Mateo et al. [11] have presented a recent study regarding the CO₂ hydrogenation under batch mode operation, where the methane production yield was 14.6 mmolCH₄ g_{cat}⁻¹ h⁻¹ (90 % of CO₂ conversion) using SrTiO₂:RuO₂ photocatalyst also at 150 °C under UV-Vis irradiation with a power of 1080 W m⁻². This output is 75 % lower equivalent to 1.02 W compared to the current study, considering the mass of the active RuO₂:TiO₂ photocatalyst (i.e., 4.7 mg) despite using an irradiance about 6.5-fold higher.

According to the DRS spectra, the RuO_{2(6.4%):TiO_{2(16.9%)}}/SBA-15 photocatalyst presents a high absorbance through whole the UV-Vis region (Fig. 5), which resulted in an apparent fraction of light absorbed by the photocatalyst of 93.7 % (average), 93.1 % and 92.6 % (estimated by Eqs. (19) and (20)), considering the wavelength interval between 280 and 800 nm (associated with the simulated sunlight), and the wavelengths of 405 nm and 365 nm (associated to the Visible and UV LEDs), respectively. The remarkable visible-light photo-responsiveness of this material can be attributed to the decline of the optical bandgap energy. That is, during the process of loading the TiO₂ semiconductor with the RuO₂ metal oxide, impurity levels are generated between the valence and conduction bands, which creates new energy levels, thus reducing the optical bandgap energy [71]. Therefore, there are slight differences between apparent photonic efficiency and apparent quantum yield, even using solar light sources. Moreover, higher photon fluxes can boost the selectivity of multi-electron photo-reactions to produce methane, ethane, and other solar fuels [72]. Even though the kinetic constant as a function of time rises with radiation intensity for all illumination sources, the amplitude was smaller for solar irradiation (Fig. 10a inside) because the RP working range permitted by the LEDs power source (0.05 W < RP < 0.55 W) was lower than for the Suntest® system (0.21 W < RP < 1.09 W). However, if we consider an RP value common to all illumination sources within the coincidental RP range (0.21 W < RP < 0.55 W), for instance, 0.4 W, the kinetic constant obtained under polychromatic irradiation was 54 % higher than those obtained for monochromatic irradiation. The better performance is

because polychromatic illumination can provide a higher number of photons at different wavelengths that can excite more reactive electrons at the different RuO₂-loaded TiO₂ energy levels, resulting in higher reaction rates. Accordingly, this material features outstanding light absorption across the solar spectrum, leading to improved spatial charge separation, directing the photogenerated electron-hole pairs to different facets [73,74].

For both monochromatic illumination sources, similar CH₄ production profiles were mostly attained, in agreement with DRS spectra (Fig. 5), being both gradually improved with the irradiance increasing (Fig. 10a.2-3 and Table 2, experiments #3.4 to #3.11), as above-mentioned, despite the photons at 365 nm being more energetic than at 405 nm [75]. According to Fujishima et al. [57], even when the photon is completely absorbed, the excess photon energy cannot be used because vibrational relaxation occurs in the upper excited state before the charge transfer occurs. Furthermore, either visible LED or UV LED could keep the CO₂ conversion at 110 min for upper irradiance values, attesting to the high photoactivity of this structured material under a wide wavelength range. Conversely, when considering the energy accumulated in the photocatalytic system, the kinetic constant for CO₂ reduction decreases as the RP increases, more sharply up to about 0.2 W (Fig. 10b, bars), in the same way as the apparent photonic efficiency (Fig. 10b, area), suggesting an excess of photons within the reactor.

It should also be noted that the structured catalytic combination of TiO₂ and RuO₂ with mesoporous SBA-15 presents a large specific surface area (as shown in Table S3), increasing light scattering and enabling the mass and photon transport inside the photocatalytic layer. These results further support the idea of designing chemically productive structured photocatalysts featuring a high capacity to collect solar photons, so solar-driven chemical reactions between photons and the catalyst can be stimulated at the microscopic level [73,74]. Considering all the above, it can be concluded that a polychromatic illumination source, like sunlight, is the most efficient regarding the nanostructured photocatalytic material here tested; however, the alternative microscale illumination by 365/405 nm LEDs is also suitable for its activation. Therefore, the polychromatic sunlight at 0.21 W, featuring the higher photonic efficiency, was selected to pursue the remaining trials.

3.2.4. Effect of the [H₂]:[CO₂] molar ratio

Besides the photocatalyst composition, the feeding composition can also affect the selectivity of the CO₂ hydrogenation reaction. Therefore, different CO₂ to H₂ molar ratios were tested (20 mg of RuO_{2(6.4%):TiO_{2(16.9%)}}/SBA-15, 150 °C, RP at 0.21 W), keeping the same CO₂ mole's number, to evaluate the reaction selectivity towards other products rather than CH₄ (Fig. 11). As expected, decreasing H₂ content by changing the [CO₂]:[H₂] molar ratio from the stoichiometric one, i.e., 1:4, to 1:2 (Table 2, experiments #3.1 and #4.1, respectively), reduced the CO₂ conversion by about 45 %. However, the formation of CO was not favoured, and the selectivity of the CO₂ hydrogenation reaction remained mainly towards CH₄ (99.8 %), being its average specific production lowered by half, with less than 0.2 % towards ethane. In the same way, when the H₂ concentration was increased by modifying the [CO₂]:[H₂] molar ratio from 1:4–1:7 (Table 2, experiments #3.1 and #4.2, respectively), the Sabatier reaction was the preferential route for the CO₂ thermo-photocatalytic conversion, with no improvement on the selectivity towards ethane generation. Also, practically the same CO₂ conversation (96 %) was attained after 110 min; still, the kinetic constant was slightly higher (about 14 %), and the CH₄ and C₂H₆ production was marginally higher (Fig. 11a, b) due to the expanded pressure in the photoreactor as well as the availability of the reducing agent. Since the carbon atom is in its higher oxidation state, CO₂ photocatalytic reduction can result in a multitude of products by the action of different numbers of electrons, which is usually reflected in low selectivity for the target compounds, adding to the challenge of separating multiple products [76]. Conversely, in this study, the selectivity of the CO₂ photocatalytic reduction towards CH₄ and C₂H₆ was maintained around

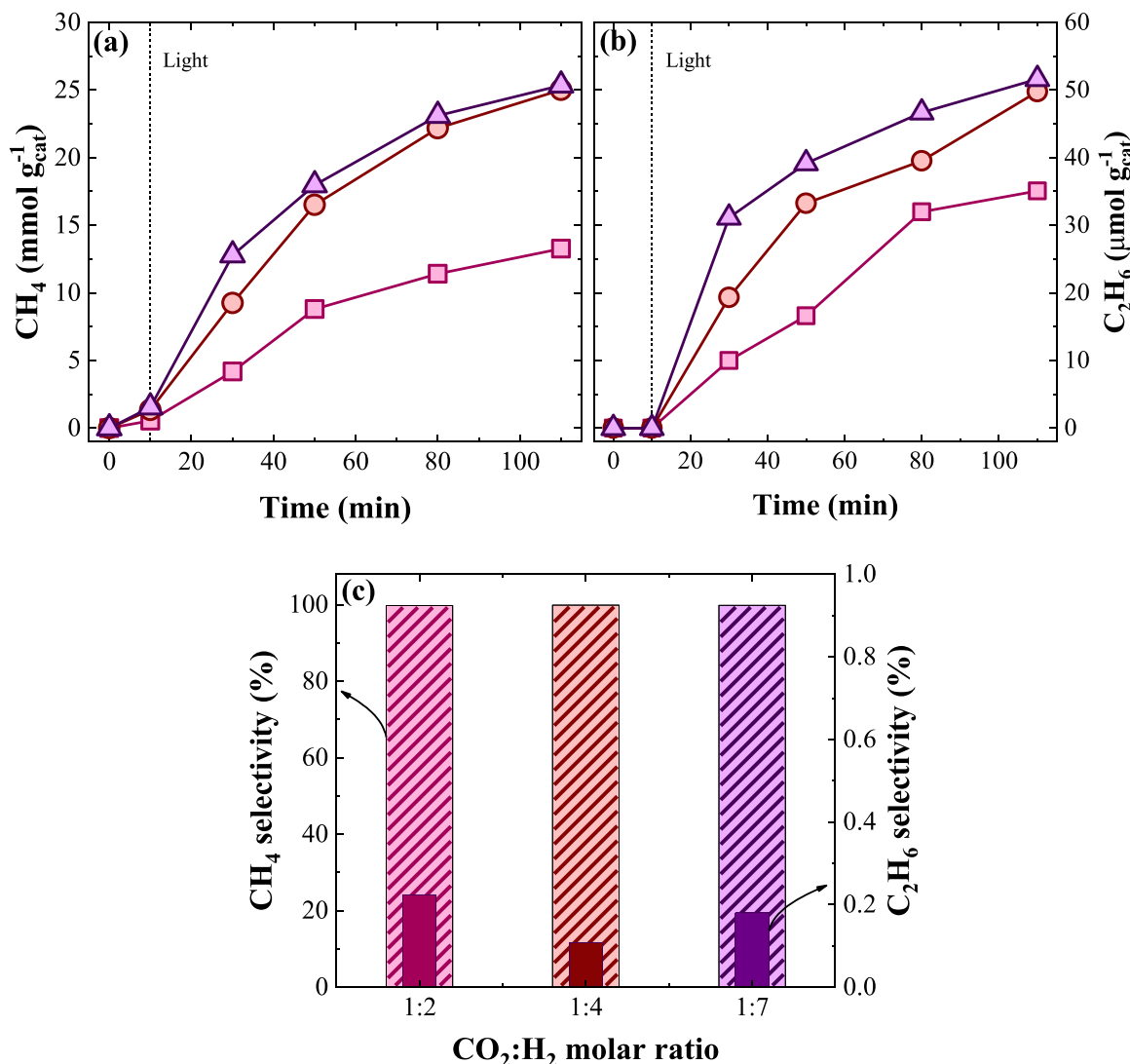


Fig. 11. Temporal profile of the solar-driven thermo-photocatalytic production of (a) CH_4 (in $\text{mmol g}_{\text{cat}}^{-1}$) and (b) ethane (in $\mu\text{mol g}_{\text{cat}}^{-1}$), along with the respective (c) product selectivity, using different $[\text{CO}_2]:[\text{H}_2]$ molar ratios: 1:2 (■); 1:4 (○); and 1:7 (△). Operating conditions: $V = 40 \text{ mL}$; $P_{\text{CO}_2} = 0.32 \text{ bar}$; $P_{\text{H}_2} = 0.64/1.28/2.24 \text{ bar}$; 20 mg of $\text{RuO}_{2(6.4\%)}:\text{TiO}_{2(16.9\%)}/\text{SBA-15}$ photocatalyst; $T = 150^\circ\text{C}$; and $RP = 0.211 \text{ W}$.

99.8 % and 0.2 % (Fig. 11c), respectively, regardless of the $\text{CO}_2:\text{H}_2$ ratio, using the novel $\text{RuO}_{2(6.4\%)}:\text{TiO}_{2(16.9\%)}/\text{SBA-15}$ nanostructured photocatalyst. Therefore, to obtain the highest CH_4 production using the lowest amount of the reducing agent, the subsequent experiments were carried out under the stoichiometric $\text{CO}_2:\text{H}_2$ molar ratio.

3.2.5. Effect of the reaction temperature

The Sabatier reaction, also known as CO_2 methanation (Eq. (22)), plays a significant role in relieving CO_2 emissions; however, to achieve high reaction yields and rates, it commonly occurs in the presence of a catalyst at temperatures above 300°C [4]. The external heating requirements can be lowered by introducing solar energy in thermal catalysis. Fig. 12a provides a comparison among the specific CH_4 production profiles for a temperature interval between 50 and 250°C , using the $\text{RuO}_{2(6.4\%)}:\text{TiO}_{2(16.9\%)}/\text{SBA-15}$ nanocomposite (20 mg catalyst, $[\text{CO}_2]:[\text{H}_2]$ molar ratio of 1:4, and RP of 0.211 W when required), under dark (Table 2, experiments #5.1 to #5.5) and light (Table 2, experiments #3.1 and #5.6 to #5.9) conditions. The $\text{RuO}_2:\text{TiO}_2$ -functionalized SBA-15 material demonstrated the ability to act concurrently as both photocatalyst and thermocatalyst. Exposure to simulated sunlight lowered the external heating demand while keeping comparable CO_2 conversion levels to those achieved at higher temperatures under dark

conditions. This improved thermo-photocatalytic performance can be ascribed to the synergistic effect between photocatalysis and thermal catalysis. In this scenario, the photo-excitation drives the reaction through an alternative transition state of low-energy, while thermal excitation acts on a new rate-determining step of dark type in the same overall sequence [77].



As expected, according to the Arrhenius law, the reaction rate increased as the temperature raised (Fig. 12), indicating that temperature favours methanation reaction kinetics, ultimately reaching CO_2 reduction efficiencies higher than 96 %. Due to the slow reaction kinetics of the methanation reaction [4], there was no significant CO_2 conversion (< 1 %) at temperatures around 50°C . Nevertheless, the initial reaction rate for CO_2 reduction was 233 % higher under simulated sunlight (experiment #5.6) than under dark conditions (experiment #5.1), indicating that thermal catalysis had negligible influence at this temperature, and the catalytic activity primarily relied on the photons' energy. It is worth noting that, the temperature of 50°C was the lowest feasible value since it coincides to the minimum temperature value that can be attained inside the Suntest's chamber. In this sense, this trial performed at 50°C under simulated sunlight can be considered as a

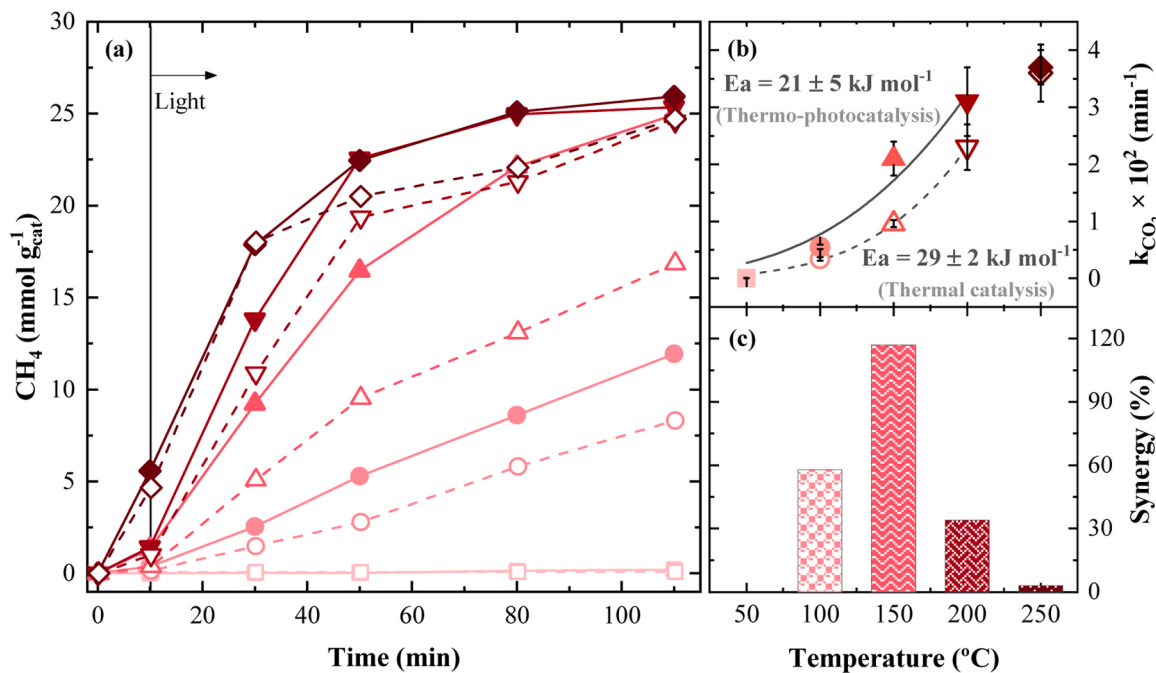


Fig. 12. (a) Temporal profile of specific CH_4 production and (b) pseudo-first-order kinetic constants for CO_2 reduction (symbols), along with Arrhenius equation fitting curves (lines) and respective apparent activation energy (E_a) values, for thermal catalysis (open symbols) and solar-driven thermo-photocatalysis (solid symbols) at different temperatures: 50 °C (—□—, —■—); 100 °C (—○—, —●—); 150 °C (—△—, —▲—); 200 °C (—▽—, —▼—); and 250 °C (—◇—, —◆—). (c) Synergy of the thermo-photocatalytic methanation process for each temperature. Operating conditions: $V = 40 \text{ mL}$; $P_{\text{CO}_2} = 0.32 \text{ bar}$; $P_{\text{H}_2} = 1.28$; 20 mg of $\text{RuO}_{2(6.4\%)}:\text{TiO}_{2(16.9\%)}:\text{SBA}-15$ photocatalyst; and $RP = 0.211 \text{ W}$ – for thermo-photocatalysis reactions.

methanation reaction via photocatalysis (without external heating). So, a pure photocatalysis process, at 50 °C and an RP of 0.21 W, resulted in a low pseudo-first order kinetic constant of $(8 \pm 1) \times 10^{-5} \text{ mM min}^{-1}$, and a low catalyst surface heating up to 73 °C after 110 min (measured by a digital infrared thermometer), indicating the existence of a limited light-to-heat conversion. However, this photothermal effect proved insufficient to activate the catalyst towards a substantial CH_4 production. In fact, by fitting the Arrhenius equation to the dark thermal catalysis, a temperature of 73 °C would lead to a reaction rate about 19-fold higher, which was not observed, further corroborating the main role of photo-mediated reactions. The low local heating of the photocatalyst surface can be attributed to the lack of infrared radiation, as the sunlight simulator configuration allows radiation to pass only between 280 and 800 nm. While UV-Vis radiation is responsible for generating charge carriers and driving photochemical reactions, the energy within the infrared spectrum, which lies beyond 780 nm, is primarily responsible for the photothermal effect, where light is converted into heat [78].

Overall, the solar-driven thermo-photocatalysis boosted the kinetic constant for CO_2 reduction concerning thermal catalysis (Fig. 12b), being more evident for the temperatures of 100, 150, and 200 °C, with increments of 62 %, 119 %, and 35 %, respectively. Considering the CO_2 conversion efficiency after 110 min, the effect of the solar light is more evident for temperatures of 100 and 150 °C, with increments of 15 % and 31 %, respectively. The catalysts' internal excitation process may have been crucial to the reaction. In this case, photogenerated charge carriers can achieve CO_2 hydrogenation via sunlight-assisted thermo-photocatalysis using TiO_2 and RuO_2 . Owing to the well-contacted interface between the RuO_2 and TiO_2 nanoparticles and the low Fermi level of RuO_2 , the photogenerated electrons can lead to the development of an electron-rich RuO_2 surface [61,64]. In turn, such a surface can produce more negative hydride, which improves the nucleophilic attack of the hydride toward the carbon core of the CO_2 molecule [61]. As the

temperature increased, the reaction rate became more dependent on the temperature than irradiation. At 250°C, the introduction of simulated sunlight had no discernible impact on the reaction kinetics, indicating that thermal catalysis dominated the reaction kinetics. Merely for temperatures between 200 and 250 °C, final CO_2 conversions higher than 98 % were achieved for thermal catalysis, even with slower kinetics than thermo-photocatalysis.

In the temperature range between 100 and 200 °C, where both thermal and photo contributions are present, the initial CO_2 reduction rate raised from 0.046 ± 0.004 – $0.30 \pm 0.05 \text{ mM min}^{-1}$ for thermal catalysis (TC, heating without light) and from 0.075 ± 0.005 – $0.41 \pm 0.08 \text{ mM min}^{-1}$ for thermo-photocatalysis (TPC, heating with light) processes (Table 2, experiments #5.2 - #5.4, and #5.7, #3.1, and #5.8). In the absence of external heating (reaction at 50 °C, which is the temperature achieved inside the Suntest's chamber), the photocatalysis (PC) process resulted in an initial CO_2 hydrogenation rate of $(1.0 \pm 0.1) \times 10^{-3} \text{ mM min}^{-1}$. These methanation performances are translated in an increase in the synergy ($r_{\text{TPC}}/(r_{\text{PC}} + r_{\text{TC}}) - 1, \%$) between thermo- and photo-catalysis from 58 % to 117 % as the temperature was increased from 100 to 150 °C, followed by a subsequent decrease up to 34 % with a further rise to 250 °C (Fig. 12c). Hence, the highest thermo-photocatalytic synergy was attained at 150 °C (Table 2, experiment #3.1), along with a CO_2 conversion of 96.8 % and an average specific CH_4 production of $13.6 \text{ mmol g}^{-1} \text{ h}^{-1}$ and $58.4 \text{ mmol g}^{-1} \text{ active cat h}^{-1}$ (with 99.8 % of selectivity for CH_4). As far as our knowledge extends, there are only a limited number of reports in the literature that demonstrate such high CO_2 photoconversion efficiencies at such low temperatures, as evidenced by the bibliographic compilation presented in Table S4. In fact, the higher specific CH_4 production rates per gram of active catalyst or loaded metal are typically reported for higher temperatures. These results further support the idea that thermo-photocatalysis mediated by renewable solar light can effectively promote CO_2 methanation at low

temperatures, especially in the presence of highly active RuO₂-loaded photocatalysts.

Fig. 12b also shows the apparent activation energy (E_a) estimated through non-linear fitting of the Arrhenius Equation (Eq. (21)) to the experimental kinetic constants for CO₂ reduction at different temperatures under dark and light conditions. Following an Arrhenius dependency, the CO₂ reduction rate rises exponentially as the temperature increases up to 200 °C/250°C for thermo-photo/thermo-catalysis. This study found an E_a value of 29 ± 2 kJ mol⁻¹ for the thermocatalytic CO₂ methanation reaction over temperature interval of 50–200 °C. Several reports have shown that the E_a is related to nanoparticles' size and dispersion of the hydrogen adsorption enthalpy [79–81]. In a study concerning CO₂ methanation reaction over a catalyst composed of Ru nanoparticles deposited onto γ-Al₂O₃, the E_a increased linearly from 42 to 117 kJ mol⁻¹ as the Ru particle size enlarged from 16 to 20 nm [81]. Considering that TEM analysis (Fig. 4) revealed that the size of the RuO₂ nanoparticles on the TiO₂/SBA-15 ranged from 5.9 to 8.6 nm, the lower E_a value obtained in the current study may be related to the smaller particle size.

Furthermore, the comparison between thermocatalytic and thermo-photocatalytic methanation within the same temperature range (50–200 °C) showed an E_a for the light-assisted process of 21 ± 5 kJ mol⁻¹

(Fig. 12b), which was 28 % lower than the E_a estimated from in-dark reactions. This declining trend in the apparent activation energy suggests that the addition of light to the thermo-catalytic process effectively lowered the energy barrier that must be overcome for the methanation reaction to occur. As a result, the reaction can proceed at a faster rate and with less energy input when both thermo- and photo-catalysis are combined, demonstrating the synergistic effect between these two catalytic mechanisms. Notwithstanding, the observed reduction in the E_a value under sunlight compared to dark conditions, along with the linear relation between methanation rate and radiant power (up to 0.75 W), indicates that the reaction mechanism is primarily driven by photon-induced hot charge carriers [70]. The photons play a crucial role in enhancing the methanation kinetics, as evidenced by the lower reaction rates obtained for low RP values (~0.05 W) via thermo-photocatalysis at 150 °C (Table 2, experiment #3.4 and #3.8) compared to the thermal catalysis at the same temperature (Table 2, experiment #5.3). Nevertheless, it is essential to note that raising the temperature up to 150 °C is also crucial to achieving high reaction yields. In this context, the novel RuO_{2(6.4%):TiO_{2(16.9%)/SBA-15}} composite not only featured thermal- and photo-catalytic activities but also demonstrates better catalytic activity than the sum of both individual activities.

In summary, the maximum temperature-irradiation synergistic effect

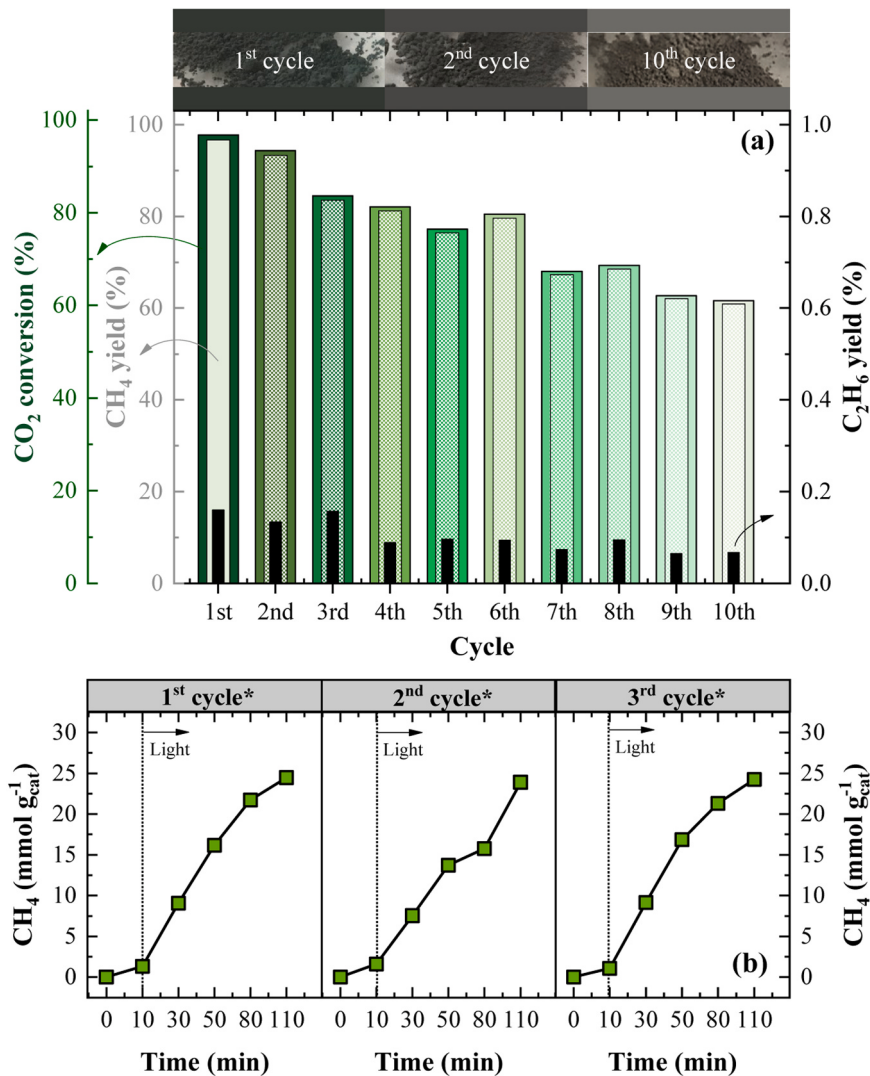


Fig. 13. Photocatalyst reusability: (a) evolution of the solar-driven thermo-photocatalytic CO₂ reduction performance along 10 sequential utilization cycles; and (b) temporal profile of specific CH₄ production along 3 consecutive utilization cycles with moist gas removal (*), by a heated N₂ stream, between them. Operating conditions: V = 40 mL; P_{CO₂} = 0.32 bar; P_{H₂} = 1.28 bar; 20 mg of RuO_{2(6.4%):TiO_{2(16.9%)/SBA-15}} photocatalyst; T = 150 °C; and RP = 0.211 W.

(117 %) was reached at 150 °C, with a reaction rate 2.2-fold higher for light-assisted CO₂ hydrogenation than the thermocatalytic one; therefore, the final reusability tests were performed at this temperature.

3.2.6. Effect of the photocatalyst reuse

Finally, the stability of the hybrid RuO_{2(6.4%)}:TiO_{2(16.9%)}/SBA-15 photocatalyst was assessed along 10 sequential utilization cycles (20 mg of RuO_{2(6.4%)}:TiO_{2(16.9%)}/SBA-15, 150 °C, [CO₂]:[H₂] molar ratio of 1:4, and RP at 0.21 W). Fig. 13a displays that the photocatalytic activity consistently diminished as the same material was being consecutively used to reduce the CO₂ into CH₄ (Table 2, experiments #3.1 #6.1 to #6.9). After 10 utilizations, methane production at 110 min decreased by 36 %, resulting from the decline of the kinetic constant for CO₂ reduction from $(2.1 \pm 0.3) \times 10^{-2} \text{ min}^{-1}$ to $(0.82 \pm 0.07) \times 10^{-2} \text{ min}^{-1}$. This phenomenon can be explained by photocatalyst poisoning, which may have occurred by the blockage of the catalyst active sites by water, a by-product of the Sabatier reaction (Eq. (22)) [82]. Such a hypothesis was proved by carrying out a reaction at the usual methanation conditions but adding 14.5 μL of UPW (considering that about 79 % of the water generated in the first cycle was retained in the reactor), which resulted in a significant drop (about 57 %) in methane production (Table 2, experiment #6.10).

During the successive photocatalyst utilisation cycles, a change in the material colour was also visually detected (Fig. 13a). As described above, FTIR analysis changed in the 3000–3757 cm⁻¹ region (Fig. 3.d), and the XPS analysis (Fig. 7a) was done to compare the fresh (Fig. 7b) and the 10-time used photocatalyst (Fig. 7c). According to the XPS survey spectrum (Fig. 7a), there was a significant increase in intensity in the O1s, Ti 2p, Si 2s, and Si 2p regions, with the most prominent changes for the O 1 s. In Si 2p spectrum (Fig. 7c.1), the peak at 105.6 eV can be associated with chemisorbed species, and the peak at 101.2 eV can be related to Si-C interaction [83]. As regards the C 1 s + Ru 3d spectrum (Fig. 7c.2), the peak at 280.9 eV, which was ascribed to the Ru-O species [84], showed a slight increment of 0.5 eV (from 280.4 to 280.9 eV) compared the fresh catalyst (Fig. 7b.2). This shift in the Ru 3d region suggests a change in the oxidative state of Ru species on the photocatalyst's surface [85], potentiated by modifications in the chemical environment, after repeated reutilization cycles. In the O 1 s region (Fig. 7c.4), a noticeable lengthening of the peak was also observed after the catalyst reuse, with the main peak at 533.5 representing the Si-O bonding in SBA-15 [54]. Another peak appeared at ca. 530.4 eV, indicating chemisorbed O₂ molecules [86], that have bonded to the material's surface. Additionally, the peak at 527.8 eV was attributed to oxygen-related defects, specifically oxygen vacancies and oxygen interstitials [87]. Oxygen vacancies occur when oxygen atoms are absent from the material's crystal lattice, while oxygen interstitials occur when oxygen atoms occupy positions within the lattice that deviate from the regular arrangement. These defects can significantly affect the material's properties, leading to the inactivation of the catalyst in the CO₂ methanation process.

Three more experiments were performed to verify if the catalyst poisoning with water could be prevented by changing the operating conditions between the thermo-photocatalytic CO₂ methanation reactions. At the end of each utilization cycle, the reactor temperature was kept at 150 °C under a nitrogen gas stream (0.2 L min⁻¹) for 30 min (Table 2, experiments #3.1, #6.11, and #6.12). Thus, the moist CH₄ was brought out of the reactor before water condensed and accumulated in the catalyst. Fig. 13b reveals that, under the abovementioned conditions, the photocatalyst presented good stability after reutilization. In this case, the CO₂ conversions stabilised from 97 % to 93 % with a kinetic constant of $(1.9 \pm 0.2) \times 10^{-2} \text{ min}^{-1}$ after three successive cycles, further supporting the hypothesis that the water is blocking the photocatalyst active sites. Contrary to what happened when the moist gas was not removed from the reactional system, where the kinetic constant was sharply reduced from $(2.1 \pm 0.3) \times 10^{-2} \text{ min}^{-1}$ to $(0.82 \pm 0.07) \times 10^{-2} \text{ min}^{-1}$ after the third utilisation cycle. Therefore, it can be inferred that

this photocatalyst can be reused if the water is removed from the system between reactions or is added an efficient water adsorbent such as zeolite 4 A [88], delaying the poisoning and the need for regeneration.

3.3. Mechanistic considerations

Fig. 14a presents a schematic diagram representing the charge-carrier separation process within both TiO_{2(18.2%)}/SBA-15 and RuO_{2(6.4%)}:TiO_{2(16.9%)}/SBA-15 nanocomposites. As previously mentioned, the DRS analysis revealed that the TiO₂/SBA-15 material has an E_g of 3.13 eV, indicating that only high-energy photons at wavelengths lower than 396 nm can promote the electrons excitation from the valence band (VB) to the conduction band (CB). As a result, the material's photocatalytic activity is limited to the solar spectrum's UV region. On the other hand, with the incorporation of plasmonic RuO₂ into the material, lattice distortion occurs, creating impurity energy levels near the VB and CB, referred to as Urbach tails [46]. The presence of these tails results in a decrease in the effective CB and an increase in the effective VB, thus reducing the effective E_g to 2.42 eV. This reduction enables the generation and separation of charge carriers, allowing electrons to be excited to the CB by absorbing low-energy visible solar photons at wavelengths lower than 512 nm (Fig. 14a).

Moreover, the heterojunction of RuO₂ with TiO₂ can lead to forming a composite featuring higher electronic conductivity, as well as Schottky barriers, which enables a charge transfer tunnelling route. As a result, electrons can efficiently be transferred from the plasmonically excited RuO₂ across the RuO₂-loaded TiO₂ heterojunction interface and exciton recombination levels can be reduced [89], leading to enhanced charge-carrier separation and utilization. When visible light is absorbed by the RuO₂:TiO₂/SBA-15 nanocomposite, hot electrons generated from the RuO₂ plasmon gain enough energy to be transferred to the material's CB. Subsequently, CO₂ molecules are reduced into CH₄ by reacting with hydrogen atoms, obtained by the H₂ dissociation on the materials' VB.

Fig. 14b illustrates a proposed reaction mechanism for CO₂ methanation over the surface of the RuO₂:TiO₂ photocatalyst, supported by relevant bibliographic data [89–92]. According to the literature, CO₂ hydrogenation into CH₄ can mainly occur via the formation of two intermediates: CO and formate. In the first pathway, the CO₂ molecule chemisorbs on the photocatalyst surface and dissociates into CO* and O* species. Then, O* reacts and is converted into water with hydrogen, and CO* dissociates into C*, being hydrogenated by the H* adsorbed on the metal surface into CH₄, which desorbs from the photocatalyst surface. In the second pathway, Ru-based photocatalyst chemisorbs H₂ and CO₂ molecules, generating formate groups followed by formic acid and then CH₄. The selectivity and product distribution in CO₂ methanation are also influenced by the different crystalline TiO₂ phases (anatase and rutile) and their respective CB positions [89,90]. When anatase TiO₂ is present, the excited electrons tend to favour the formation of CO, which is more energetically demanding, over the formation of CH₄ [89,93]. In this way, as the RuO₂:TiO₂/SBA-15 material developed in the current work contains anatase in its formulation and no other reaction products were detected apart from CH₄ and C₂H₆ (< 0.2 %), it was assumed that the primary pathway for CO₂ methanation reaction involved the formation of CO as an intermediate. This pathway also can lead to the formation of CH₃* species, which further reacts to form C₂H₆. The higher selectivity found for CH₄ rather than C₂H₆ may be related to its higher redox potential, which should be more positive than the CB edge position.

It is worth mentioning that, as a supporting material, SBA-15 provides a large surface area, ensuring a uniform distribution of the photocatalyst's active sites over its surface, as observed by the SEM and TEM images. Such an innovative configuration has the ability to minimise the shading effects and charge recombination, leading to enhanced light absorption and efficient electron transfer reactions. As a result of this well-designed approach, the nanostructured RuO_{2(6.4%)}:TiO_{2(16.9%)}/SBA-15 composite effectively converts solar energy into a usable fuel,

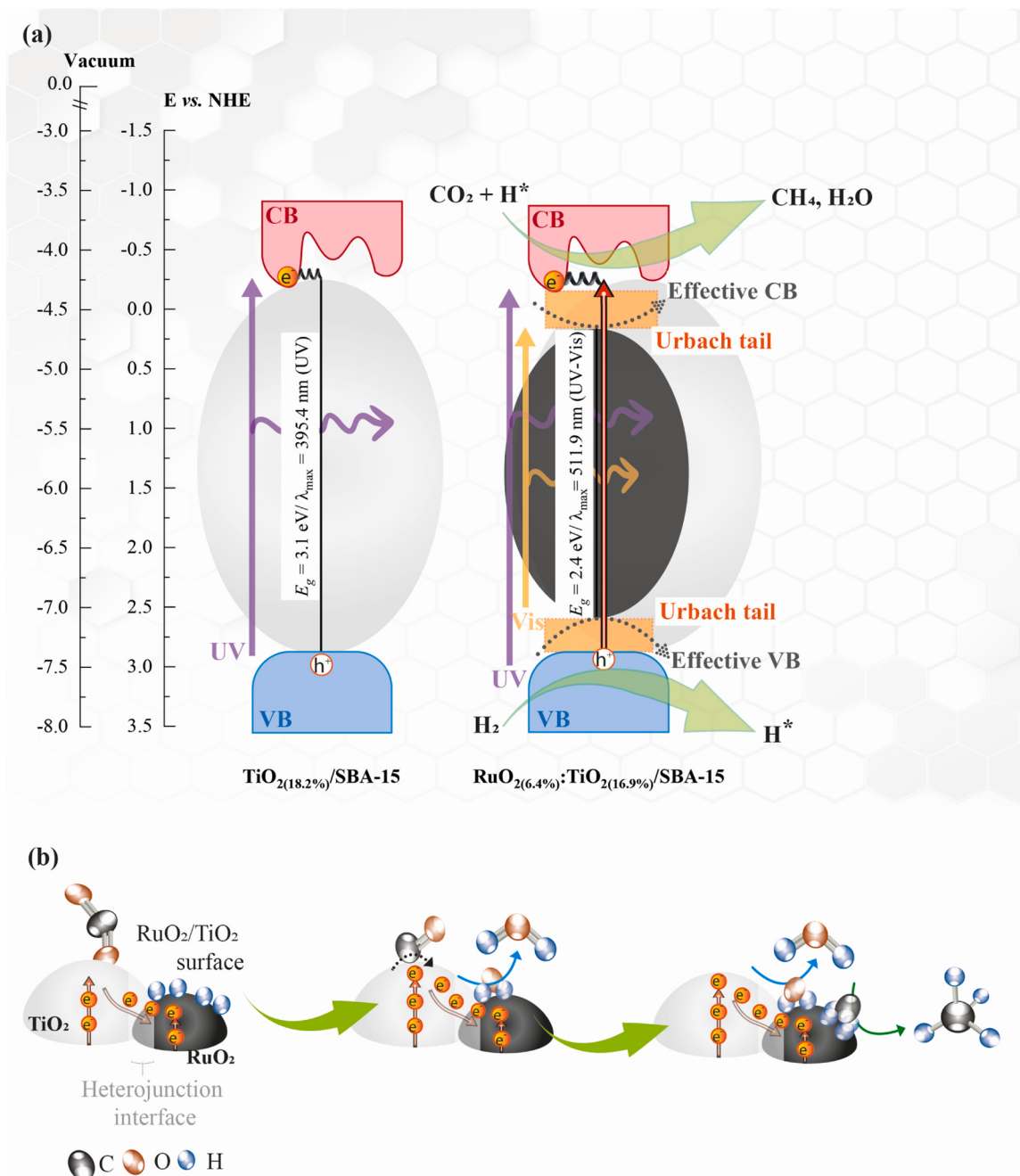


Fig. 14. Schematic illustration representing (a) the narrowing of the effective optical band gap energy from the $\text{TiO}_{2(18.2\%)}/\text{SBA-15}$ to $\text{RuO}_{2(6.4\%)}:\text{TiO}_{2(16.9\%)}/\text{SBA-15}$ material due to the effect of the Urbach tails (adapted from [46]) and (b) the proposed mechanism for the reduction of CO_2 into CH_4 over the $\text{RuO}_2:\text{TiO}_2$ surface (based on [89,90]).

achieving a 96.8 % thermo-photocatalytic CO_2 conversion efficiency and a 42.1 % apparent quantum yield at a lower temperature (150 °C) than conventional processes. Considering that only 23.3 % of the material (TiO_2 and RuO_2) is actually photoactive, the specific CH_4 production rate increases by about 4-fold, resulting in $58.6 \text{ mmol g}_{\text{active_cat}}^{-1} \text{ h}^{-1}$, which is among the highest values reported. This outstanding performance highlights its potential for CO_2 valorisation, with great implications for sustainable solar-to-chemical energy conversion processes.

4. Conclusions

A novel $\text{RuO}_{2(6.4\%)}:\text{TiO}_{2(16.9\%)}/\text{SBA-15}$ material was successfully applied to promote solar-driven thermo-photocatalytic CO_2

hydrogenation, reaching a CH_4 production of $59.7/58.6 \text{ mmol g}_{\text{active_cat}}^{-1} \text{ h}^{-1}$ ($13.9/13.6 \text{ mmol g}_{\text{cat}}^{-1} \text{ h}^{-1}$ or $286.1/280.7 \text{ mmol g}_{\text{Ru}}^{-1} \text{ h}^{-1}$), with a 99.8/99.8 % selectivity and a 99.4/96.8 % CO_2 conversion at 150 °C, using an RP of 0.45/0.21 W, respectively. The excellent performance of this hybrid nanostructured thermo-photocatalyst was correlated with its high surface area, boosting the light-harvesting, active surface sites, and mass transfer. The process was driven at a significantly lower temperature (150 °C) than the conventional catalytic methanation process (300–500 °C) due to the thermo-photocatalytic approach. Adding the RuO_2 metal oxide to the $\text{TiO}_2/\text{SBA-15}$ composite was essential to attain a material able to absorb light across the solar spectrum, resulting in high methanation yields. Under polychromatic solar radiation, the photocatalytic material presented the best photo-responsiveness, attaining an apparent photonic efficiency and

an apparent quantum yield of 39.5 % and 42.1 %, respectively, with a radiation power of 0.21 W. Notwithstanding, the monochromatic illumination through 365/405 nm LEDs can be a suitable alternative to the sunlight. Moreover, it was also inferred that even with a fluctuation in the H₂ supply, the selectivity of the RuO_{2(6.4%)}:TiO_{2(16.9%)}/SBA-15 photocatalyst towards methane remained high (99.8 %) and constant. Finally, the photoactivity declined by 36 % after 10 cycles owing to active sites' blockage by water, but if water was removed between trials, the photocatalytic activity remained virtually constant.

CRediT authorship contribution statement

Larissa O. Paulista: Investigation, Validation, Visualization, Formal analysis, Writing-original draft, Writing-review & editing. **Alexandre F. P. Ferreira:** Conceptualization; Supervision; Writing - review and editing. **Bruna Castanheira:** Material preparation, Writing-review and editing. **Maja B. Đolić:** Material characterization, Writing-review and editing. **Ramiro J.E. Martins:** Funding acquisition; Supervision; Writing - review and editing. **Rui A. Boaventura:** Funding acquisition; Supervision; Writing - review and editing. **Vítor J.P. Vilar:** Conceptualization; Funding acquisition; Supervision; Writing - review and editing. **Tânia F.C.V. Silva:** Conceptualization; Funding acquisition; Supervision; Writing - review and editing.

Declaration of Competing Interest

The authors declare that they have no known competing financial interests or personal relationships that could have appeared to influence the work reported in this paper.

Data Availability

The authors are unable or have chosen not to specify which data has been used.

Acknowledgements

This work was financially supported by: (i) LA/P/0045/2020 (ALICE), UIDB/50020/2020 and UIDP/50020/2020 (LSRE-LCM), funded by national funds through *Fundação para a Ciência e a Tecnologia (FCT)*, and *Ministério da Ciência, Tecnologia e Ensino Superior (MCTES)*, Portugal, under *Programa de Investimento e Despesas de Desenvolvimento da Administração Central (PIDAAC)*; (ii) project HyGreen&LowEmissions (NORTE-01-0145-FEDER-000077), supported by Norte Portugal Regional Operational Programme (NORTE 2020), under the PORTUGAL 2020 Partnership Agreement, through the European Regional Development Fund (ERDF); and (iii) project CO2-to-CH4 (2022.01176. PTDC), supported by national funds through the FCT/MCTES (PIDAAC). Larissa O. Paulista acknowledges the Ph.D. fellowship supported by FCT (reference SFRH/BD/137639/2018 and COVID/BD/152922/2022). Maja B. Đolić acknowledges the Ministry of Education, Science and Technological Development of the Republic of Serbia (Contract No. 451-03-9/2022-14/200135). Tânia F.C.V. Silva acknowledges the FCT Individual Call to Scientific Employment Stimulus 2017 (CEECIND/01386/2017).

Appendix A. Supporting information

Supplementary data associated with this article can be found in the online version at doi:10.1016/j.apcatb.2023.123232.

References

- [1] Intergovernmental Panel on Climate Change (IPCC), Climate Change 2022: Impacts, Adaptation and Vulnerability, 2022.
- [2] S.L. Wong, B.B. Nyakuma, A.H. Nordin, C.T. Lee, N. Ngadi, K.Y. Wong, O. Oladokun, Uncovering the dynamics in global carbon dioxide utilization research: a bibliometric analysis (1995–2019), Environ. Sci. Pollut. Res. 28 (2021) 13842–13860.
- [3] M. Thema, F. Bauer, M. Sterner, Power-to-gas: electrolysis and methanation status review, Renew. Sustain. Energy Rev. 112 (2019) 775–787.
- [4] M. Aziz, A. Jalil, S. Triwahyono, A. Ahmad, CO₂ methanation over heterogeneous catalysts: recent progress and future prospects, Green. Chem. 17 (2015) 2647–2663.
- [5] A. Olivo, E. Ghedini, M. Signoretto, M. Compagnoni, I. Rossetti, Liquid vs. gas phase CO₂ photoreduction process: which is the effect of the reaction medium? Energies 10 (2017) 1394.
- [6] F. Zhang, Y.-H. Li, M.-Y. Qi, Y.M.A. Yamada, M. Anpo, Z.-R. Tang, Y.-J. Xu, Photothermal catalytic CO₂ reduction over nanomaterials, Chem. Catal. (2021).
- [7] M. Khalil, J. Gunlaizuardi, T.A. Ivandini, A. Umar, Photocatalytic conversion of CO₂ using earth-abundant catalysts: a review on mechanism and catalytic performance, Renew. Sustain. Energy Rev. 113 (2019), 109246.
- [8] D.G. Nocera, Solar fuels and solar chemicals industry, Acc. Chem. Res. 50 (2017) 616–619.
- [9] H. Huang, J. Zhao, Y. Du, C. Zhou, M. Zhang, Z. Wang, Y. Weng, J. Long, J. Hofkens, J.A. Steele, M.B.J. Roeflaers, Direct Z-scheme heterojunction of semicoherent FAPbBr₃/Bi₂WO₆ interface for photoredox reaction with large driving force, ACS Nano 14 (2020) 16689–16697.
- [10] M. Tschurl, Semiconductor/metal (oxide) hybrid materials for applications in photocatalysis, in: K. Wandelt (Ed.), Encyclopedia of Interfacial Chemistry, Elsevier, Oxford, 2018, pp. 573–580.
- [11] D. Mateo, J. Albero, H. García, Titanium-perovskite-supported RuO₂ nanoparticles for photocatalytic CO₂ methanation, Joule 3 (2019) 1949–1962.
- [12] D. Wang, R. Huang, W. Liu, D. Sun, Z. Li, Fe-based MOFs for photocatalytic CO₂ reduction: Role of coordination unsaturated sites and dual excitation pathways, ACS Catal. 4 (2014) 4254–4260.
- [13] Fd.C. da Silva, Md.S. Costa, L. da Silva, A. Batista, G. da Luz, Functionalization methods of SBA-15 mesoporous molecular sieve: a brief overview, SN Appl. Sci. 1 (2019) 1–11.
- [14] R. Chen, X. Cheng, X. Zhu, Q. Liao, L. An, D. Ye, X. He, Z. Wang, High-performance optofluidic membrane microreactor with a mesoporous CdS/TiO₂/SBA-15@carbon paper composite membrane for the CO₂ photoreduction, Chem. Eng. J. 316 (2017) 911–918.
- [15] P. Zhou, J. Yu, M. Jaroniec, All-solid-state Z-scheme photocatalytic systems, Adv. Mater. 26 (2014) 4920–4935.
- [16] X. Huang, J. Wang, T. Li, J. Wang, M. Xu, W. Yu, A. El Abed, X. Zhang, Review on optofluidic microreactors for artificial photosynthesis, Beilstein J. Nanotechnol. 9 (2018) 30–41.
- [17] H. Ishida, Electrochemical/photochemical CO₂ reduction catalyzed by transition metal complexes, Carbon Dioxide Chemistry, Capture and Oil Recovery, IntechOpen, London, 2018.
- [18] F.J. Trindade, G.J. Fernandes, A.S. Araújo, V.J. Fernandes Jr, B.P. Silva, R. Nagayasu, M.J. Politi, F.L. Castro, S. Brochsztajn, Covalent attachment of 3, 4, 9, 10-peryleneediimides onto the walls of mesoporous molecular sieves MCM-41 and SBA-15, Microporous Mesoporous Mater. 113 (2008) 463–471.
- [19] D. Zhao, J. Feng, Q. Huo, N. Melosh, G.H. Fredrickson, B.F. Chmelka, G.D. Stucky, Triblock copolymer syntheses of mesoporous silica with periodic 50 to 300 angstrom pores, Science 279 (1998) 548–552.
- [20] B. Castanheira, L. Otubo, C.L.P. Oliveira, R. Montes, J.B. Quintana, R. Rodil, S. Brochsztajn, V.J.P. Vilar, A.C.S.C. Teixeira, Functionalized mesoporous silicas SBA-15 for heterogeneous photocatalysis towards CECs removal from secondary urban wastewater, Chemosphere 287 (2022), 132023.
- [21] Y.J. Acosta-Silva, R. Nava, V. Hernández-Morales, S.A. Macías-Sánchez, M. L. Gómez-Herrera, B. Pawelec, Methylene blue photodegradation over titania-decorated SBA-15, Appl. Catal. B: Environ. 110 (2011) 108–117.
- [22] L.O. Paulista, J. Albero, R.J. Martins, R.A. Boaventura, V.J. Vilar, T.F. Silva, H. García, Turning carbon dioxide and ethane into ethanol by solar-driven heterogeneous photocatalysis over RuO₂-and NiO-co-doped SrTiO₃, Catalysts 11 (2021) 461.
- [23] J. Hong, W. Zhang, J. Ren, R. Xu, Photocatalytic reduction of CO₂: a brief review on product analysis and systematic methods, Anal. Methods 5 (2013) 1086–1097.
- [24] A. Salinaro, A.V. Emeline, J. Zhao, H. Hidaka, V.K. Ryabchuk, N. Serpone, Terminology, relative photonic efficiencies and quantum yields in heterogeneous photocatalysis. Part II: experimental determination of quantum yields, Pure Appl. Chem. 71 (1999) 321–335.
- [25] S.H. Bossmann, E. Oliveros, S. Göb, S. Siegwart, E.P. Dahlen, L. Payawan, M. Straub, M. Wörner, A.M. Braun, New evidence against hydroxyl radicals as reactive intermediates in the thermal and photochemically enhanced Fenton reactions, J. Phys. Chem. A 102 (1998) 5542–5550.
- [26] A.I. Gomes, T.F.C.V. Silva, M.A. Duarte, R.A.R. Boaventura, V.J.P. Vilar, Cost-effective solar collector to promote photo-Fenton reactions: a case study on the treatment of urban mature leachate, J. Clean. Prod. 199 (2018) 369–382.
- [27] R.W. Frei, J.D. MacNeil, Diffuse Reflectance Spectroscopy in Environmental Problem-Solving, CRC press., 2019.
- [28] H. Kisch, D. Bahnmann, Best practice in photocatalysis: comparing rates or apparent quantum yields? J. Phys. Chem. Lett. (2015).
- [29] M.M. Araújo, L.K.R. Silva, J.C. Sczancoski, M.O. Orlandi, E. Longo, A.G.D. Santos, J.L.S. Sá, R.S. Santos, G.E. Luz, L.S. Cavalcante, Anatase TiO₂ nanocrystals anchored at inside of SBA-15 mesopores and their optical behavior, Appl. Surf. Sci. 389 (2016) 1137–1147.
- [30] Z. Wang, F. Zhang, Y. Yang, B. Xue, J. Cui, N. Guan, Facile postsynthesis of visible-light-sensitive titanium dioxide/mesoporous SBA-15, Chem. Mater. 19 (2007) 3286–3293.

- [31] L.M. Carvalho, A.F. Soares-Filho, M.S. Lima, J.F. Cruz-Filho, T.C. Dantas, G.E. Luz, 2, 4-Dichlorophenoxyacetic acid (2, 4-D) photodegradation on $\text{WO}_3\text{-TiO}_2\text{-SBA-15}$ nanostructured composite, Environ. Sci. Pollut. Res. 28 (2021) 7774–7785.
- [32] L. Liu, Y. Li, Understanding the reaction mechanism of photocatalytic reduction of CO_2 with H_2O on TiO_2 -based photocatalysts: a review, Aerosol air Qual. Res. 14 (2014) 453–469.
- [33] L. Yang, Z. Jiang, S. Lai, C. Jiang, H. Zhong, Synthesis of titanium containing SBA-15 and its application for photocatalytic degradation of phenol, Int. J. Chem. Eng. 2014 (2014).
- [34] V. Natarajan, S. Basu, Performance and degradation studies of $\text{RuO}_2\text{-Ta}_2\text{O}_5$ anode electrocatalyst for high temperature PBI based proton exchange membrane water electrolyser, Int. J. Hydrog. Energy 40 (2015) 16702–16713.
- [35] P. Joshi, D. Sutrade, A comparative study of structural and morphological properties of pristine and Mn doped ruthenium oxide thin films, Int. J. Thin Films Sci. Technol. 6 (2017) 83–86.
- [36] R. Viter, I. Iatsunskyi, Optical spectroscopy for characterization of metal oxide nanofibers, Handb. Nanofibers 5 (2018) 1–35.
- [37] S. Kumaravel, S. Thiripuranthagan, M. Durai, E. Erusappan, T. Vembuli, Catalytic transfer hydrogenation of biomass-derived levulinic acid to γ -valerolactone over Sn/Al-SBA-15 catalysts, N. J. Chem. 44 (2020) 8209–8222.
- [38] D.R. Sahu, L. Hong, S.-C. Wang, J.-L. Huang, Synthesis, analysis and characterization of ordered mesoporous $\text{TiO}_2\text{/SBA-15}$ matrix: effect of calcination temperature, Microporous Mesoporous Mater. 117 (2009) 640–649.
- [39] D. Zhao, Q. Huo, J. Feng, B.F. Chmelka, G.D. Stucky, Nonionic triblock and star diblock copolymer and oligomeric surfactant syntheses of highly ordered, hydrothermally stable, mesoporous silica structures, J. Am. Chem. Soc. 120 (1998) 6024–6036.
- [40] Q. Qi, T. Zhang, X. Zheng, L. Wan, Preparation and humidity sensing properties of Fe-doped mesoporous silica SBA-15, Sens. Actuators B: Chem. 135 (2008) 255–261.
- [41] J. Tauc, Optical properties and electronic structure of amorphous Ge and Si, Mater. Res. Bull. 3 (1968) 37–46.
- [42] C. Zhao, L. Liu, Q. Zhang, J. Wang, Y. Li, Photocatalytic conversion of CO_2 and H_2O to fuels by nanostructured Ce-TiO₂/SBA-15 composites, Catal. Sci. Technol. 2 (2012) 2558–2568.
- [43] M. Capel-Sánchez, J. Campos-Martín, J. Fierro, M. De Frutos, A.P. Polo, Effective alkene epoxidation with dilute hydrogen peroxide on amorphous silica-supported titanium catalysts, Chem. Commun. (2000) 855–856.
- [44] M.Q. Yang, M. Gao, M. Hong, G.W. Ho, Visible-to-NIR photon harvesting: progressive engineering of catalysts for solar-powered environmental purification and fuel production, Adv. Mater. 30 (2018) 1802894.
- [45] J. Singh, V. Verma, R. Kumar, R. Kumar, Influence of Mg²⁺-substitution on the optical band gap energy of Cr_{2-x}Mg_xO₃ nanoparticles, Results Phys. 13 (2019), 102106.
- [46] N. Khatun, E.G. Rini, P. Shirage, P. Rajput, S.N. Jha, S. Sen, Effect of lattice distortion on bandgap decrement due to vanadium substitution in TiO₂ nanoparticles, Mater. Sci. Semicond. Process. 50 (2016) 7–13.
- [47] R. Gunasekaran, J. Charles, Synthesis, structural, morphological and optical analyses of new Prussian blue, ruthenium oxide and polyindole (PIn-PB-RuO₂) nanocomposite, J. Polym. Res. 29 (2022) 381.
- [48] R. Thahir, A.W. Wahab, N.L. Nafie, I. Raya, Synthesis of high surface area mesoporous silica SBA-15 by adjusting hydrothermal treatment time and the amount of polyvinyl alcohol 17 (2019) 963–971.
- [49] H. Zhang, M. Li, P. Xiao, D. Liu, C.-J. Zou, Structure and catalytic performance of Mg-SBA-15-supported nickel catalysts for CO₂ reforming of methane to syngas, J. Chem. Eng. Technol. 36 (2013) 1701–1707.
- [50] S.-j Kim, Y.K. Cho, J. Seok, N.-S. Lee, B. Son, J.W. Lee, J.M. Baik, C. Lee, Y. Lee, M. H. Kim, Highly branched RuO₂ nanoneedles on electrospun TiO₂ nanofibers as an efficient electrocatalytic platform, ACS Appl. Mater. Interfaces 7 (2015) 15321–15330.
- [51] P. Zhang, Y. Sui, Y. Wang, Z. Wang, J. Zhao, N. Wen, H. Chen, H. Huang, Z. Zhang, R. Yuan, Z. Ding, W. Dai, X. Fu, Y.-X. Wang, J. Long, Surface Ru-H bipyridine complexes-grafted TiO₂ nanohybrids for efficient photocatalytic CO₂ methanation, J. Am. Chem. Soc. 145 (2023) 5769–5777.
- [52] H. Zhang, P. Zhang, J. Zhao, Y. Liu, Y. Huang, H. Huang, C. Yang, Y. Zhao, K. Wu, X. Fu, S. Jin, Y. Hou, Z. Ding, R. Yuan, M.B.J. Roefraers, S. Zhong, J. Long, The Hole-Tunneling Heterojunction of Hematite-Based Photoanodes Accelerates Photosynthetic Reaction 60 (2021) 16009–16018.
- [53] E. Guedes, F. Abud, H. Martins, M. Abbate, R. Jardim, R. Mossanek, Role of Ti-Ru interaction in $\text{SrTi}_{0.5}\text{Ru}_{0.5}\text{O}_3$: physical properties, x-ray spectroscopy, and cluster model calculations, Phys. Rev. B 100 (2019), 075132.
- [54] N. Zhong, H. Shima, H. Akinaga, Mechanism of the performance improvement of TiO₂-x-based field-effect transistor using SiO₂ as gate insulator, AIP Adv. 1 (2011).
- [55] J.L.G. Fierro, M.A. Peña, L. González Tejuca, An XPS and reduction study of PrCo_3 , J. Mater. Sci. 23 (1988) 1018–1023.
- [56] Y. Tang, L. Dong, S. Mao, H. Gu, T. Malkoske, B. Chen, Enhanced photocatalytic removal of tetrabromobisphenol A by magnetic CoO@graphene nanocomposites under visible-light irradiation, ACS Appl. Energy Mater. 1 (2018) 2698–2708.
- [57] A. Fujishima, T.N. Rao, D.A. Tryk, Titanium dioxide photocatalysis, J. Photochem. Photobiol. C: Photochem. Rev. 1 (2000) 1–21.
- [58] J.L. White, M.F. Baruch, J.E. Pander III, Y. Hu, I.C. Fortmeyer, J.E. Park, T. Zhang, K. Liao, J. Gu, Y. Yan, Light-driven heterogeneous reduction of carbon dioxide: photocatalysts and photoelectrodes, Chem. Rev. 115 (2015) 12888–12935.
- [59] V.D. Patake, C.D. Lokhande, Chemical synthesis of nano-porous ruthenium oxide (RuO_2) thin films for supercapacitor application, Appl. Surf. Sci. 254 (2008) 2820–2824.
- [60] M.M. Steeves, Electronic transport properties of ruthenium and ruthenium dioxide thin films, The University of Maine., 2011.
- [61] B. Jin, X. Ye, H. Zhong, F. Jin, Y.H. Hu, Enhanced photocatalytic CO₂ hydrogenation with wide-spectrum utilization over black TiO₂ supported catalyst, Chin. Chem. Lett. 33 (2022) 812–816.
- [62] V. Subramanian, E. Wolf, P.V. Kamat, Semiconductor– metal composite nanostructures. To what extent do metal nanoparticles improve the photocatalytic activity of TiO₂ films? J. Phys. Chem. B 105 (2001) 11439–11446.
- [63] C.-C. Yang, J. Vernimmen, V. Meynen, P. Cool, G. Mul, Mechanistic study of hydrocarbon formation in photocatalytic CO₂ reduction over Ti-SBA-15, J. Catal. 284 (2011) 1–8.
- [64] S. Al-Shomar, Investigation the effect of doping concentration in Ruthenium-doped TiO₂ thin films for solar cells and sensors applications, Mater. Res. Express 7 (2020), 036409.
- [65] M. Ismael, Highly effective ruthenium-doped TiO₂ nanoparticles photocatalyst for visible-light-driven photocatalytic hydrogen production, N. J. Chem. 43 (2019) 9596–9605.
- [66] S. Al Jitan, G. Palmisano, C. Garlisi, Synthesis and surface modification of TiO₂-based photocatalysts for the conversion of CO₂, Catalysts 10 (2020) 227.
- [67] B.M. da Costa Filho, V.J.P. Vilar, Strategies for the intensification of photocatalytic oxidation processes towards air streams decontamination: a review, Chem. Eng. J. 391 (2020), 123531.
- [68] S. Sorcar, S. Yoriya, H. Lee, C.A. Grimes, S.P. Feng, A review of recent progress in gas phase CO₂ reduction and suggestions on future advancement, Mater. Today Chem. 16 (2020), 100264.
- [69] M.A.L.R.M. Cortes, J.W.J. Hamilton, P.K. Sharma, A. Brown, M. Nolan, K.A. Gray, J.A. Byrne, Formal quantum efficiencies for the photocatalytic reduction of CO₂ in a gas phase batch reactor, Catal. Today 326 (2019) 75–81.
- [70] D. Mateo, J.L. Cerrillo, S. Durini, J. Gascon, Fundamentals and applications of photo-thermal catalysis, Chem. Soc. Rev. (2021).
- [71] R. Ameta, M.S. Solanki, S. Benjamin, S.C. Ameta, Chapter 6 - photocatalysis, in: S. C. Ameta, R. Ameta (Eds.), Advanced Oxidation Processes for Waste Water Treatment, Academic Press, 2018, pp. 135–175.
- [72] V. Singh, I.J.C. Beltran, J.C. Ribot, P. Nagpal, Photocatalysis deconstructed: design of a new selective catalyst for artificial photosynthesis, Nano Lett. 14 (2014) 597–603.
- [73] S. Han, Y. Chen, S. Abanades, Z. Zhang, Improving photoreduction of CO₂ with water to CH₄ in a novel concentrated solar reactor, J. Energy Chem. 26 (2017) 743–749.
- [74] A. Bachmeier, S. Hall, S.W. Ragsdale, F.A. Armstrong, Selective visible-light-driven CO₂ reduction on a p-type dye-sensitised NiO photocathode, J. Am. Chem. Soc. (2014) 179–191.
- [75] G. Liao, C. Li, X. Li, B. Fang, Emerging polymeric carbon nitride Z-scheme systems for photocatalysis, Cell Rep. Phys. Sci. (2021), 100355.
- [76] J. Fu, K. Jiang, X. Qiu, J. Yu, M. Liu, Product selectivity of photocatalytic CO₂ reduction reactions, Mater. Today 32 (2020) 222–243.
- [77] N. Keller, J. Ivanez, J. Highfield, A.M. Ruppert, Photo-/thermal synergies in heterogeneous catalysis: towards low-temperature (solar-driven) processing for sustainable energy and chemicals, Appl. Catal. B: Environ. 296 (2021), 120320.
- [78] Z. Wang, Z. Yang, R. Fang, Y. Yan, J. Ran, L. Zhang, A. State-of-the-art, review on action mechanism of photothermal catalytic reduction of CO₂ in full solar spectrum, Chem. Eng. J. 429 (2022), 132322.
- [79] M. Kuśmierz, Kinetic study on carbon dioxide hydrogenation over Ru/ γ -Al₂O₃ catalysts, Catal. Today 137 (2008) 429–432.
- [80] R. Narayan, T. King, Hydrogen adsorption states on silica-supported Ru–Ag and Ru–Cu bimetallic catalysts investigated via microcalorimetry, Thermochim. Acta 312 (1998) 105–114.
- [81] S. Navarro-Jáen, J.C. Navarro, L.F. Bobadilla, M.A. Centeno, O.H. Laguna, J. A. Odriozola, Size-tailored Ru nanoparticles deposited over γ -Al₂O₃ for the CO₂ methanation reaction, Appl. Surf. Sci. 483 (2019) 750–761.
- [82] L.B. Hoch, T.E. Wood, P.G. O'Brien, K. Liao, L.M. Reyes, C.A. Mims, G.A. Ozin, The rational design of a single-component photocatalyst for gas-phase CO₂ reduction using both UV and visible light, Adv. Sci. 1 (2014) 1400013.
- [83] L. Sun, C. Han, N. Wu, B. Wang, Y. Wang, High temperature gas sensing performances of silicon carbide nanosheets with an n–p conductivity transition, RSC Adv. 8 (2018) 13697–13707.
- [84] Q.T. Le, E. Güll Arslan, J. Rip, H. De Coster, P. Verdonck, D. Radisic, F. Schleicher, I. Vaesen, T. Conard, E. Altamirano-Sánchez, Studying the efficacy of hydrogen plasma treatment for enabling the etching of thermally annealed ruthenium in chemical solutions, Micro Nano Eng. 19 (2023), 100208.
- [85] D. Foix, M. Sathiya, E. McCalla, J.-M. Tarascon, D. Gonbeau, X-ray photoemission spectroscopy study of cationic and anionic redox processes in high-capacity Li-ion battery layered-oxide electrodes, J. Phys. Chem. C 120 (2016) 862–874.
- [86] L. Zeng, W. Song, M. Li, D. Zeng, C. Xie, Catalytic oxidation of formaldehyde on surface of HTiO₂/HCTiO₂ without light illumination at room temperature, Appl. Catal. B: Environ. 147 (2014) 490–498.
- [87] Y. Luo, L. Cao, L. Feng, J. Huang, L. Yang, C. Yao, Y. Cheng, Synthesis, characterization and photocatalytic properties of nanoscale pyrochlore type Bi₂Zr₂O₇, Mater. Sci. Eng.: B 240 (2019) 133–139.
- [88] W. Zhu, L. Gora, A.W.C. van den Berg, F. Kapteijn, J.C. Jansen, J.A. Moulijn, Water vapour separation from permanent gases by a zeolite-4A membrane, J. Membr. Sci. 253 (2005) 57–66.
- [89] E. Morais, C. O'Modhrain, K.R. Thampi, J.A. Sullivan, RuO₂/TiO₂ photocatalysts prepared via a hydrothermal route: influence of the presence of TiO₂ on the reactivity of RuO₂ in the artificial photosynthesis reaction, J. Catal. 401 (2021) 288–296.

- [90] J. Riga, C. Tenret-Noël, J.J. Pireaux, R. Caudano, J.J. Verbist, Y. Gobillon, Electronic structure of rutile oxides TiO_2 , RuO_2 and IrO_2 studied by X-ray photoelectron spectroscopy, *Phys. Scr.* 16 (1977) 351.
- [91] K. Jalama, Carbon dioxide hydrogenation over nickel-, ruthenium-, and copper-based catalysts: Review of kinetics and mechanism, *Catal. Rev.* 59 (2017) 95–164.
- [92] F. Solymosi, A. Erdöhelyi, M. Kocsis, Methanation of CO_2 on supported Ru catalysts, *J. Chem. Soc., Faraday Trans. 1: Phys. Chem. Condens. Phases* 77 (1981) 1003–1012.
- [93] J. Zhou, Z. Gao, G. Xiang, T. Zhai, Z. Liu, W. Zhao, X. Liang, L. Wang, Interfacial compatibility critically controls Ru/ TiO_2 metal-support interaction modes in CO_2 hydrogenation, *Nat. Commun.* 13 (2022) 327.